International Journal of Biological Macromolecules 375 (2026) 153422

Contents lists available at ScienceDirect

International Journal of Biological Macromolecules

journal homepage: www.elsevier.com/locate/ijbiomac

Geometry-dependent interfaces shape NLRP3 pyrin domain assembly

Mehri Javid [a], Alexander Dömling [b], Maryam Nikkhah [c], Grzegorz Popowicz [d], Mohammad Hashemabadi [e], Ahmad Reza Shahverdi [a], Zargham Sepehrizadeh [a], Azadeh Ebrahim-Habibi [a,f,*], Saman Hosseinkhani [g,**]

[a] Department of Pharmaceutical Biotechnology, Faculty of Pharmacy, Tehran University of Medical Sciences, Tehran, Iran
[b] Institute of Molecular and Translational Medicine, Faculty of Medicine and Dentistry, and Czech Advanced Technology and Research Institute, Palacky University, Olomouc, Czech Republic
[c] Department of Nanobiotechnology, Faculty of Biological Sciences, Tarbiat Modares University, Tehran, Iran
[d] Helmholtz Zentrum München, Neuherberg, Germany
[e] Department of Cellular and Molecular Biology, Faculty of Life science and Biotechnology, Shahid beheshti university, Tehran, Iran
[f] Biosensor Research Center and Endocrinology and Metabolism Research Center, Endocrinology and Metabolism Molecular-Cellular Sciences Institute, Tehran University of Medical Sciences, Tehran, Iran
[g] Department of Biochemistry, Faculty of Biological Sciences, Tarbiat Modares University, Tehran, Iran

ARTICLE INFO

Keywords:
NLRP3 inflammasome
Pyrin domain (PYD)
Protein–protein interactions
Interfacial geometry
Homotypic PYD assembly
CAPS-associated mutations
Molecular dynamics simulations
Structure-guided modulation

ABSTRACT

NLRP3 inflammasome activation requires precise regulation of pyrin domain (PYD)-mediated protein–protein interactions to prevent spontaneous self-association while enabling rapid ASC adaptor recruitment. However, how local PYD interfaces encode the balance between restrained and assembly-competent states remains unclear. Here, we combine structural analysis, atomistic molecular dynamics simulations, targeted mutagenesis, heterotypic native/mutant split-luciferase complementation, ASC recruitment assays, microscale thermophoresis, and mass photometry to define geometry-dependent regulation of NLRP3 PYD self-association. A key feature of this work is the use of heterotypic native/mutant PYD pairings, enabling systematic comparison of interfacial, peripheral, and dual mutations and revealing interaction modes not accessible in homogeneous wild-type or mutant systems.

We identify two distinct PYD–PYD geometries: a Type A-like restrained, non-filamentous dimeric contact and a Type B-like filament-compatible geometry that preserves the canonical Ia–Ib interface observed in active inflammasome assemblies. Both retain the six-helix PYD fold, indicating that functional differences arise primarily from interfacial organization rather than global structural changes. Residue-level perturbations further show that regulatory and CAPS-associated mutations remodel PYD assembly through distinct mechanisms. The S5D phosphomimetic substitution exhibits position- and orientation-dependent effects, being tolerated in permissive contexts but disrupting filament-compatible organization in sensitive interfaces. D31V decouples adaptor docking from higher-order assembly, whereas D21H reshapes restrained Type A-like interactions while preserving assembly competence.

Together, these findings establish NLRP3 PYD self-association as a geometry-dependent process governed by electrostatic, hydrogen-bonding, and hydrophobic networks. This framework provides structural insight into regulatory modifications and CAPS-associated mutations and highlights PYD interfaces as potential targets for structure-guided modulation of NLRP3 inflammasome signaling.

1. Introduction

Supramolecular signaling platforms rely on precisely regulated protein–protein interfaces that govern the transition between restrained and assembly-competent states. The NOD-like receptor family pyrin domain-containing protein 3 (NLRP3) inflammasome exemplifies this principle, functioning as a central innate immune scaffold that converts diverse pathogenic and endogenous danger cues into caspase-1

* Correspondence to: A. Ebrahim-Habibi, Department of Pharmaceutical Biotechnology, Faculty of Pharmacy, Tehran University of Medical Sciences, Tehran, Iran.
** Corresponding author.
E-mail addresses: aehabibi@sina.tums.ac.ir (A. Ebrahim-Habibi), saman_h@modares.ac.ir (S. Hosseinkhani).

https://doi.org/10.1016/j.ijbiomac.2026.153422
Received 15 May 2026; Received in revised form 29 June 2026; Accepted 7 July 2026
Available online 9 July 2026

activation and pyroptotic cell death [1,2]. Aberrant NLRP3 activation is causally linked to multiple inflammatory and neurodegenerative disorders, including multiple sclerosis, type 2 diabetes, rheumatoid arthritis, and Alzheimer's disease [3,4], and gain-of-function mutations give rise to cryopyrin-associated periodic syndromes (CAPS) [5]. These observations underscore the sensitivity of this pathway to subtle structural perturbations and establish NLRP3 as a high-value therapeutic target [3,6]. However, the structural mechanisms that prevent spontaneous assembly while preserving rapid activation competence remain incompletely defined.

NLRP3 activation proceeds through a biphasic mechanism comprising priming followed by higher-order assembly [1,7,8]. Priming promotes transcriptional upregulation and multiple post-translational modifications, including phosphorylation, ubiquitination, sumoylation, and acetylation, while maintaining the receptor in an autoinhibited state [9–12]. A subsequent activation signal induces oligomerization through the NACHT and pyrin domains (PYD), enabling heterotypic PYD–PYD recruitment of the adaptor ASC and downstream filament formation [1,13,14]. Recent studies further indicate that acetylation-sensitive lysines in the N-terminal PYD region contribute to NLRP3 oligomerization- and ASC-associated assembly, suggesting that PTMs can tune PYD interface behavior as well as upstream licensing [11,12]. Although upstream signaling pathways have been extensively characterized, the molecular determinants that couple relief of autoinhibition to productive PYD nucleation remain unresolved. In particular, how the PYD suppresses spontaneous polymerization under basal conditions yet transitions rapidly to an assembly-competent state upon stimulation is not structurally understood.

The PYD occupies a central position in this regulatory transition. Phosphorylation of defined PYD residues during priming suppresses premature assembly, whereas acetylation-sensitive N-terminal PYD lysines have been linked to NLRP3 oligomerization and ASC-associated assembly [11,12,15]. These observations suggest that chemically distinct PTMs can tune PYD assembly through different effects on local interfacial chemistry. Upon activation, the PYD mediates homotypic NLRP3 interactions that nucleate ASC polymerization and amplify signaling [16]. Structurally, the PYD adopts a conserved six-helix bundle characteristic of the death-domain superfamily, conferring an intrinsic propensity for self-association [16]. This inherent associativity complicates discrimination between productive and non-productive interfaces and has limited high-resolution insight into functionally relevant assembly geometries [17]. Increasing evidence suggests that PYD assembly reflects a dynamic ensemble of alternative interfacial arrangements rather than a single static interface [8,16]. Within such a landscape, structurally observed non-filamentous PYD–PYD contacts may represent restrained geometries that limit spontaneous propagation, whereas filament-compatible geometries can support ASC recruitment and downstream assembly after activation [18,19]. Accordingly, point mutations or post-translational modifications, including phosphorylation [15] and acetylation [11,12], may modulate the relative population of these interfacial geometries by changing local electrostatic and hydrophobic surface properties [20].

Resolving how positional perturbations reshape PYD interfacial organization requires approaches capable of capturing transient, geometry-dependent interface behavior beyond static structural snapshots. All-atom molecular dynamics simulations enable analysis of interfacial dynamics, contact persistence, and configurational sampling [18,19,21,22], whereas quantitative biophysical assays provide complementary measurements of homotypic PYD interactions [23–25]. Here, we integrate atomistic simulations with targeted mutagenesis and complementary interaction analyses to define the structural determinants that distinguish alternative PYD assembly geometries. A distinguishing feature of our experimental design is the direct interrogation of heterotypic native/mutant PYD pairings, which enables resolution of interface behavior not accessible through homogeneous systems alone. We identify two structurally distinct homotypic PYD–PYD geometries that differ in topology, compactness, and compatibility with filament-associated propagation. Perturbation of discrete interface residues reshapes these geometries in a position-dependent manner, thereby modulating adaptor accessibility and assembly behavior. Together, these findings support a model in which NLRP3 PYD assembly is governed by geometry-dependent interfacial organization within a conserved six-helix scaffold. This framework provides a mechanistic basis for understanding how regulatory and disease-associated perturbations bias PYD assemblies toward restrained versus filament-compatible states.

2. Materials & methods

2.1. Protein interfaces analysis

A homology search was performed using NCBI BLASTP [26], restricted to entries in the Protein Data Bank (PDB), using the human NLRP3 PYD sequence as the query. Human structures exhibiting 100% sequence identity to NLRP3 PYD and reported PYD–PYD interactions were selected for structural analysis. Interfacial contacts within these structures were identified and visualized using YASARA Structure (version 22.9.24) [27].

To assess the evolutionary conservation of residues involved in PYD-mediated interactions, non-redundant orthologous sequences of NLRP3 PYD were retrieved using PSI-BLAST [28]. Multiple sequence alignment was performed using MAFFT (version 7) with default parameters [29], and residue conservation at the identified interfaces was visualized using WebLogo [30].

2.2. Protein-protein docking

Homotypic docking of the NLRP3 PYD was performed using the HADDOCK web server [31]. The rationale for this docking step was to generate standardized pairwise PYD–PYD models that could be compared directly within the overall methodological design of the study. The Type A-like reference geometry is intrinsically dimer-like, whereas the published Type B-like NLRP3 PYD filament architecture contains multiple asymmetric pairwise interface classes, including Ia–Ib, IIa–IIb, and IIIa–IIIb. Because the subsequent computational and experimental analyses were designed around defined pairwise PYD–PYD comparisons, a representative dimer-level Type B-like contact was required for direct comparison with the Type A-like dimer. This pairwise reduction was not intended to imply that the full Type B-like filament is formed by a single isolated contact, that Ia–Ib is the first contact formed during assembly, or that it is thermodynamically dominant in isolation. Rather, it provided a standardized model for testing how local interfacial geometry and mutation placement influence pairwise PYD association behavior.

In this study, docking was not used as a de novo structure prediction method, thermodynamic estimator, or physical ranking of interface stability. Instead, HADDOCK was used as a restraint-guided model-generation and interface-geometry consistency tool to reconstruct experimentally derived PYD–PYD contact geometries under a standardized modeling framework. Docking scores were therefore interpreted only as empirical, model-dependent HADDOCK compatibility metrics used for internal comparison and interface prioritization, not as ΔG values, binding affinities, or evidence that one interface is thermodynamically favored over another.

Representative chains directly extracted from PDB entries 3QF2 (chains A and B) [15] and 7PZD (chains O, R, and T) [14] were used to define Type A-like and Type B-like geometrical restraints, respectively. Active residues were defined based on interfacial contacts observed in the corresponding reference structures. In the Type A-like configuration, docking restraints were applied to residues Glu^{30}, Asp^{31}, Arg^{43}, Gly^{44}, Glu^{47}, and Lys^{48} on one subunit, and Met^{27}, Glu^{30}, Asp^{31}, Arg^{43}, Gly^{44}, Glu^{47}, and Lys^{48} on the opposing subunit. For Type B-like candidate

geometries, interaction restraints were defined across six complementary filament-associated interfacial surfaces: Ia (Met^3, Ser^5, Arg^7, Cys^8, Ala^{11}, Val^{52}, Asp^{53}, Thr^{56}), Ib (Lys^{23}, Lys^{24}, Met^{27}, His^{28}, Glu^{30}, Asp^{31}, Lys^{36}), IIa (Ile^{39}, Asp^{60}, Phe^{61}), IIb (Asn^{79}, Arg^{80}, Arg^{81}, Asp^{82}), IIIa (Pro^{42}, Arg^{43}, Gly^{44}, Gln^{45}, Glu^{47}), and IIIb (Glu^{15}, Asp^{16}, Glu^{18}, Asp^{19}). All remaining parameters were kept at the default HADDOCK settings. Docking solutions were clustered using the standard HADDOCK protocol, and cluster selection was based on cluster score, cluster size, restraint satisfaction, and geometric consistency as internal HADDOCK criteria, rather than on thermodynamic interpretation or absolute energetic ranking.

2.3. Molecular dynamic simulation

To investigate the structural dynamics of the two reference PYD–PYD geometries, chains A and B from PDB structure 3QF2 [17] were selected as a Type A-like non-filamentous/restrained reference model, and chains O and R from PDB structure 7PZD [16] were selected as a Type B-like filament-compatible reference model. Point mutations (S5D, D31V, and D21H) were individually introduced into both Type A-like and Type B-like assemblies using the SwapRes command in YASARA Structure (v22.9.24) [27]. Depending on the assembly geometry, each mutation was positioned at the interaction interface, at a peripheral region, or spanning both contexts. Side-chain conformations were optimized using the SCWALL method under the YASARA2 force field [32], followed by a short relaxation step using the default YASARA minimization protocol prior to production simulations.

Molecular dynamics simulations were performed using the AMBER14 force field [33] implemented in YASARA Structure [27]. Protonation states of titratable residues were assigned based on pKa predictions at physiological pH [34], Each system was solvated in a cubic simulation box containing 0.9% (*w/v*) NaCl aqueous solution, with a minimum solute-to-box distance of 20 Å, and solvent density adjusted to 0.997 $g{\cdot}mL^{-1}$. Long-range electrostatic interactions were treated using the Particle Mesh Ewald (PME) method [35], with an 8 Å cutoff applied to short-range nonbonded interactions. Simulations were conducted under periodic boundary conditions with constrained hydrogen atoms and a 2.5 fs integration time step, maintaining a temperature of 298 K and a pressure of 1 bar in the NPT ensemble [36]. Each native and mutant PYD–PYD assembly model was simulated as a single 100 ns production trajectory. Therefore, trajectory-derived dispersions reported for simulation metrics represent frame-to-frame fluctuations within the same trajectory.

Trajectory snapshots were extracted every 100 ps and analyzed using the md_analyze macro in YASARA to compute Cα root-mean-square deviation (Cα-RMSD), radius of gyration, per-residue root-mean-square fluctuation (RMSF), and time-resolved secondary structure profiles. Coordinated residue motions were quantified using a Dynamic Cross-Correlation Map (DCCM) based on Cα displacement vectors according to:

$$\mathrm{DCCM}_{ij} = \frac{\langle \vec{d}_i \cdot \vec{d}_j \rangle}{\left(\langle \left| \vec{d}_i \right|^2 \rangle \langle \left| \vec{d}_j \right|^2 \rangle \right)^{1/2}}$$

where $\vec{d}_i$ and $\vec{d}_j$ represent displacement vectors of atoms *i* and *j* from their respective average positions, and angle brackets denote time-averaging over all trajectory frames. Interface interaction–solvation scores between the two PYD monomers were calculated using the YASARA md_analyzebindenergy macro. For each dimer, one monomer was operationally assigned as the receptor and the other as the protein ligand, and the same object definition, force field, solvation model, trajectory sampling interval, and analysis protocol were applied to all native and mutant Type A-like and Type B-like systems. The md_analyzebindenergy output was reported using the native YASARA sign convention as an MM/PBSA-like interaction–solvation score [37]. These values are not thermodynamic binding free energies, do not include conformational entropy or standard-state corrections, and should not be interpreted as absolute ΔG values, Kd values, or direct binding affinities. Within this strictly comparative framework, shifts toward more negative or less negative values were interpreted only as model-dependent descriptors of interfacial persistence, compactness, and solvent exposure within the same analysis workflow, without implying thermodynamic preference or quantitative energetic ranking.

2.4. Recombinant plasmid construction

Wild-type and S5D mutant constructs of NLuc-PYD and CLuc-PYD cloned into pET28a(+) (Kanˆ R; Novagen, Germany) were obtained from our previous work [25]. Additional PYD variants (D31V and D21H) were generated by site-directed mutagenesis using mutation-specific primers (Table S1) and Phusion high-fidelity DNA polymerase (New England Biolabs, USA). Following *Dpn*I digestion (Takara Bio, Japan) to remove methylated parental templates, PCR products were transformed into *Escherichia coli* DH5α for plasmid propagation. All introduced mutations were verified by Sanger sequencing using an ABI 3130xl Genetic Analyzer (Thermo Fisher Scientific) (Fig. S1).

For coexpression assays, NLuc-PYD and CLuc-PYD variants were assembled into the dual-expression vector pETDuet-1 (Ampˆ R; Novagen), which contains two independent T7 promoters and multiple cloning sites (MCS1 and MCS2). Internal *Nde*I and *Xba*I restriction sites within the NLuc-PYD sequence were removed by silent mutagenesis to facilitate sequential cloning. The modified NLuc-PYD fragment was amplified and inserted into MCS1 via NdeI/*Xho*I restriction sites, followed by insertion of PCR-amplified CLuc-PYD into MCS2 using XbaI/*Hin*dIII. Point mutations (D31V and D21H) were subsequently introduced into one or both PYD copies using a one-step overlapping PCR mutagenesis strategy. Because identical PYD sequences are present in both NLuc-PYD and CLuc-PYD, mutagenic primers could anneal to either copy, enabling generation of multiple mutant combinations within a single PCR reaction (Fig. S2). Reaction products included full-length circular plasmids containing the desired mutations, which were identified by colony PCR based on their expected band patterns. Double-mutant constructs were generated by re-cloning CLuc-PYD fragments carrying the first mutation into vectors containing the second mutation in NLuc-PYD. All final constructs (Fig. S3) were confirmed by Sanger sequencing prior to use in coexpression experiments. Together, this construct panel enabled systematic testing of heterotypic native/mutant PYD pairings and positional mutation placement in both individually expressed and co-expressed reporter configurations (Fig. S3).

2.5. Protein expression and purification

Small-scale expression of NLuc- and CLuc-tagged constructs was performed in *Escherichia coli* BL21-CodonPlus (DE3)-RIPL cells (Agilent, USA). Cultures were grown in LB medium supplemented with 50 μg/mL kanamycin and chloramphenicol at 37 °C to an optical density at 600 nm (OD_{600}) of approximately 0.6, induced with 0.5 mM IPTG, and further incubated at 20 °C for 6 h. Cells were harvested by centrifugation, resuspended in lysis buffer (20 mM Tris–HCl, 500 mM NaCl, 20 mM imidazole, pH 7.8), and lysed by sonication (10 min total, 10 s on/20 s off). Lysates were clarified by centrifugation at 15,000 ×*g* for 20 min at 4 °C. For soluble constructs, the supernatant was applied to a Ni–NTA affinity column (Qiagen), washed with buffer containing 40 mM imidazole, and eluted with 275 mM imidazole. In contrast, CLuc–ASC was predominantly recovered as inclusion bodies. The insoluble fraction was washed to remove residual soluble proteins, solubilized in denaturing buffer (8 M urea, 20 mM Tris–HCl, 500 mM NaCl, 20 mM imidazole, pH 7.8), and clarified by centrifugation. The denatured protein was purified using Ni–NTA affinity chromatography on a Bio-Rad FPLC system and refolded on-column by applying a linear urea gradient from 8 M to 0 M.

After washing with denaturing buffer containing 40 mM imidazole, refolded protein was eluted with 275 mM imidazole. Protein purity and integrity were assessed by SDS–PAGE, and purified proteins were either used immediately or stored at −80 °C until further use.

2.6. Luciferase activity assay

In vitro luciferase activity was measured by mixing 20 μL of purified NLuc- or CLuc-tagged protein with 20 μL of One-Glo™ Luciferase Assay Substrate (Promega) in white 96-well plates. Luminescence signals were recorded immediately at room temperature using an EnSpire Multimode Plate Reader (PerkinElmer). To ensure quantitative comparability across samples, luminescence intensities were normalized to protein concentrations determined by the Bradford assay (Bio-Rad, USA). All quantitative experiments were performed in at least three independent biological replicates ($n \geq 3$), and data are presented as mean ± standard deviation (SD). Statistical significance was assessed using ordinary one-way ANOVA followed by Dunnett's multiple-comparisons test against the corresponding control group. Statistical significance thresholds were defined as $p < 0.05$ (*), $p < 0.01$ (**), $p < 0.001$ (***), and $p < 0.0001$ (****).

2.7. Microscale thermophoresis

Apparent soluble low-order association between CLuc-PYD interaction pairs, including CLuc-PYD/CLuc-PYD (native/native), CLuc-PYD/CLuc-PYD S5D (native/S5D), and CLuc-PYD S5D/CLuc-PYD S5D (S5D/S5D), was evaluated using microscale thermophoresis (MST). CLuc-PYD and CLuc-PYD S5D proteins were fluorescently labeled with NT-647 dye (NanoTemper Technologies, Germany) according to the manufacturer's instructions. Labeled proteins were used at a fixed final concentration of 50 nM and titrated against serial dilutions of the corresponding unlabeled binding partners in PBS supplemented with 0.05% (*v*/v) Tween-20. MST measurements were performed at 25 °C using standard capillaries on a Monolith NT.115 instrument (NanoTemper Technologies) with 50% LED power. Concentration-dependent MST responses were analyzed using the built-in Kd model in MO.Affinity Analysis software (NanoTemper Technologies), and the software-reported values were reported as apparent dissociation constants (K_d,app). Because NLRP3 PYD is assembly-prone, these K_d,app values represent operational estimates of soluble low-order PYD–PYD association under the specific assay conditions, and are not interpreted as absolute microscopic thermodynamic constants or as direct measurements of filament formation.

2.8. Mass photometry

Mass photometry (MP) was used to assess the soluble low-order oligomeric distributions of CLuc-PYD and its S5D and D31V variants. This assay was applied to compare apparent molecular-mass distributions of soluble CLuc-fused PYD species under the tested conditions and was not used as a direct filament-formation assay. Purified proteins were stored at −80 °C and thawed on ice immediately prior to measurements.

Experiments were performed at room temperature using a MassGlass instrument (Refeyn, UK). For each measurement, 20 μL of protein sample were applied to a clean glass coverslip, and the corresponding elution buffer was used for sample dilution and background correction. Data acquisition and analysis were performed using AcquireMP and DiscoverMP software, respectively. Molecular-mass calibration was performed using MFP1 and bovine serum albumin (BSA) standards, providing reference peaks in the 66–344 kDa range for accurate assignment of particle masses.

Because MP detects individual particles in solution, the resulting mass distributions represent apparent soluble oligomeric states under the specific assay conditions and are not interpreted as measurements of filament assembly, polymerization efficiency, or absolute equilibrium populations.

3. Results

3.1. Alternative PYD interfaces define topologically distinct assembly geometries

The molecular determinants that enable NLRP3 PYD self-association while preventing aberrant inflammasome activation remain incompletely resolved. The PYD adopts a conserved six-helix bundle that presents six canonical interaction surfaces—Ia, Ib, IIa, IIb, IIIa, and IIIb—capable of mediating homotypic assembly. Structural survey and integrative modeling of available human NLRP3 PYD-containing assemblies indicated that these surfaces can organize into two topologically distinct PYD–PYD contact geometries (Table 1).

The first geometry, referred to here as Type A-like, is represented by the isolated NLRP3 PYD crystal contact in 3QF2 [17] and by a compatible PYD-dimer arrangement reported within the inactive CRID3-bound full-length NLRP3 decamer/cage structure, 7PZC [8]. In this geometry, an Ib-containing surface is engaged within a dimer-like contact, consistent with a restrained/non-filamentous arrangement. The second geometry, referred to as Type B-like, corresponds to the NLRP3 PYD filament architecture represented by 7PZD [16] and to active inflammasome disk structures such as 8ERT [38], in which complementary Ia–Ib surfaces remain organized for repetitive PYD addition and ASC recruitment. Thus, Type A-like contacts are treated here as non-filamentous/restrained geometries with possible regulatory relevance, whereas Type B-like is defined as the filament-compatible geometry.

To generate standardized PYD–PYD models for downstream comparison, candidate Type A-like and Type B-like pairwise geometries were reconstructed using reference-guided HADDOCK restraints derived from experimentally observed PYD–PYD contacts. Because these restraints were defined from reference structures, the docking analysis was not used as an unbiased search or as independent thermodynamic evidence. Instead, HADDOCK provided an internal, model-dependent compatibility metric for identifying restraint-satisfying interface geometries suitable for subsequent molecular dynamics simulations and mutational analyses.

The Type A-like reference model corresponded to a dimer-like IIIa–Ib contact involving Met,[27] Glu,[30] Asp,[31] Arg[43], Gly[44], Glu[47], and Lys[48]. In contrast, the published Type B-like NLRP3 PYD filament architecture contains multiple asymmetric pairwise interfaces, including Ia–Ib, IIa–IIb, and IIIa–IIIb. Among these candidate Type B-like pairwise contacts, Ia–Ib was selected as the representative dimer-level Type B-like geometry for downstream analysis because it corresponds to the interface organization emphasized in published NLRP3 PYD filament and active inflammasome disk structures, displayed the largest buried surface area among the tested Type B-like pairings, and included conserved and functionally relevant residues, including Met,[3] Ser,[5] Arg,[7] Cys,[8] Ala,[11] Lys,[23] Lys,[24] Met,[27] His,[28] Glu,[30] Asp,[31] Lys,[36] Val[52], Asp[53], and Thr[56] (Table 2; Fig. 1). HADDOCK scores are reported in Table 2 as empirical, model-dependent compatibility metrics within the HADDOCK framework and were not interpreted as physical binding free energies, thermodynamic rankings, or evidence for the temporal order of interface formation during filament assembly.

To assess the dynamic behavior of these reference geometries beyond static docking, all-atom molecular dynamics simulations were performed on representative dimers derived from PDB structures 3QF2 (Type A-like) and 7PZD (Type B-like). Both assemblies retained global secondary structure throughout the simulations (Fig. S4). Type B-like dimers exhibited lower average Cα RMSD (1.45 ± 0.25 Å) relative to Type A-like dimers (2.45 ± 0.53 Å) (Fig. 2A) and reduced radius of gyration (18.38 ± 0.15 Å versus 20.63 ± 0.42 Å, respectively; Fig. 2B), consistent with greater compactness. The YASARA-derived MM/PBSA-like interaction–solvation scores were also more negative for the Type B-like model (−893 ± 96.61 kJ mol^{-1}) than for the Type A-like model (−433.37 ± 105.00 kJ mol^{-1}) (Fig. 3). These values are used only as comparative, trajectory-derived descriptors of interfacial persistence

Table 1
Human NLRP3 pyrin domain (PYD)-containing structures used to define reference PYD–PYD interaction geometries.

Accession code	Structural determination method	Aggregation state/assembly	Resolution (Å)	Schematic representation	Reference
3QF2	X-Ray diffraction	Particle/isolated PYD dimer	1.7		[17]
7PZD	Electron microscopy	Filament/NLRP3 PYD filament	3.60	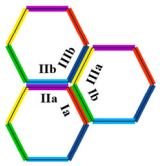	[16]
7PZC	Electron microscopy	Particle/inactive CRID3-bound full-length NLRP3 decamer with resolved PYD dimer	3.90		[8]
8ERT	Electron microscopy	Filament/active-disc NLRP3 PYD filament	3.30	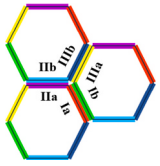	[38]

Table 2
Reference-guided HADDOCK compatibility metrics for NLRP3 PYD–PYD interface models.

Interface	HADDOCK score	vDW (kcal/mol)	Electrostatics (kcal/mol)	BSA (Å^2)
Type B Ia–Ib	−90.7 ± 0.9	−26.1 ± 2.9	−357.1 ± 26.1	1138.6 ± 52.0
Type A IIIa–Ib	−66.6 ± 1.7	−18.4 ± 3.1	−312.5 ± 19.8	952.3 ± 41.2
Type B IIa–IIb	−52.3 ± 1.4	−14.7 ± 2.5	−198.4 ± 15.6	784.1 ± 38.9
Type B IIIa–IIIb	−48.9 ± 1.2	−12.6 ± 2.1	−176.3 ± 14.2	721.5 ± 35.7

and compactness within the same scoring framework and are not interpreted as physical binding free energies, absolute thermodynamic affinities, or energetic rankings. Interface-resolved analysis (Table 3; Fig. 4A,C) indicated that the Type B-like model maintained an extended hydrogen-bond network across the Ia–Ib interface, whereas the Type A-like model relied more heavily on discrete ionic contacts. Consistently, RMSF analysis revealed reduced backbone flexibility in the Type B-like model, particularly across helices 2 and 3 (Fig. 2C).

Together, these analyses define two reference PYD–PYD geometries that differ in topology, compactness, contact persistence, and model-dependent dynamic behavior despite preservation of the global six-helix scaffold.

Phosphomimetic S5D Perturbs PYD Assembly in a Position-Dependent Manner.

Phosphorylation of Ser^5 has been reported to suppress NLRP3 filament formation by disrupting the Ser^5–Asp^{31} hydrogen bond at the Ia–Ib interface [15]. To assess how geometric context modulates this perturbation, S5D phosphomimetic substitutions were introduced into both type A and type B assemblies and evaluated by molecular dynamics simulations.

In the type A configuration, where Ser^5 is non-interfacial on both monomers (Fig. 1), S5D substitutions produced moderate destabilization without catastrophic structural disruption. Single and dual S5D variants increased Cα root-mean-square deviation (RMSD) to 3.02 ± 0.69 Å and 3.35 ± 1.23 Å, respectively (Fig. 2 AI), relative to wild type. Interaction scores changed to −471.35 ± 83.74 kJ mol^{-1} and −388.47 ± 96.51 kJ mol^{-1} for the single and dual substitutions, respectively (Fig. 3I). (Fig. 3I), whereas radius of gyration (Rg) remained largely unchanged (Fig. 2 BI). Secondary structure analysis revealed localized helix-to-coil transitions in residues 42–49 in the dual variant and turn-to-3$_{10}$-helix transitions in residues 33–36 in the single variant (Fig. S5B). Despite these local perturbations, core IIIa–Ib interfacial contacts—including Met,[27] Glu,[30] Asp,[31] Arg[43], Gly[44], Glu[47], and Lys[48]—remained largely preserved (Fig. 4B; Table 3). These data indicate that S5D substitution is structurally tolerated within the type A geometry.

In contrast, the type B configuration—characterized by one interfacial Ser^5 hydrogen-bonded to Asp^{31} and one peripheral Ser^5 (Fig. 1)—was highly sensitive to phosphomimetic substitution. Interfacial S5D markedly increased Cα-RMSD (4.47 ± 1.92 Å) and RMSF (3.65 ± 1.12 Å) (Fig. 2 AI, CI), reduced intersubunit contact frequency (Table 3; Fig. 4D), and shifted the interaction score to −530.48 ± 137.04 kJ mol^{-1} (Fig. 3I). Dual S5D substitutions further amplified destabilization (−671.67 ± 171.26 kJ mol^{-1}). By contrast, peripheral S5D substitution in type B produced minimal changes in RMSD (1.71 ± 0.27 Å) and interaction score (−805.87 ± 104.25 kJ mol^{-1}). In this configuration, ionic interactions involving Glu,[30] Asp,[31] and Arg[43] partially compensated for local perturbation, and increased flexibility was largely confined to helix 3 (Fig. S6; Table 3). Together, these results demonstrate pronounced positional asymmetry in S5D tolerance within the type B interface.

To assess functional consequences, split-luciferase complementation assays were performed (Figs. 5–6). Because the Type B configuration is asymmetric—unlike the symmetric Type A arrangement—it permits two alternative assembly orientations within the biosensor system (Fig. 5I). S5D substitution was therefore used as a positional probe to discriminate between these geometries. Introduction of S5D into NLuc-PYD abolished luminescence in both NLuc-PYD S5D/CLuc-PYD and NLuc-PYD S5D/CLuc-PYD S5D combinations. In contrast, the reciprocal NLuc-PYD/CLuc-PYD S5D pairing retained and modestly increased signal relative to the native interaction (Fig. 5I). These data identify the Ia interface contributed by NLuc-PYD as important for reporter compatible Type B-like complementation and support Model II as the orientation compatible with efficient luciferase fragment reconstitution. Peripheral S5D substitution in type B (NLuc-PYD/CLuc-PYD S5D) preserved high

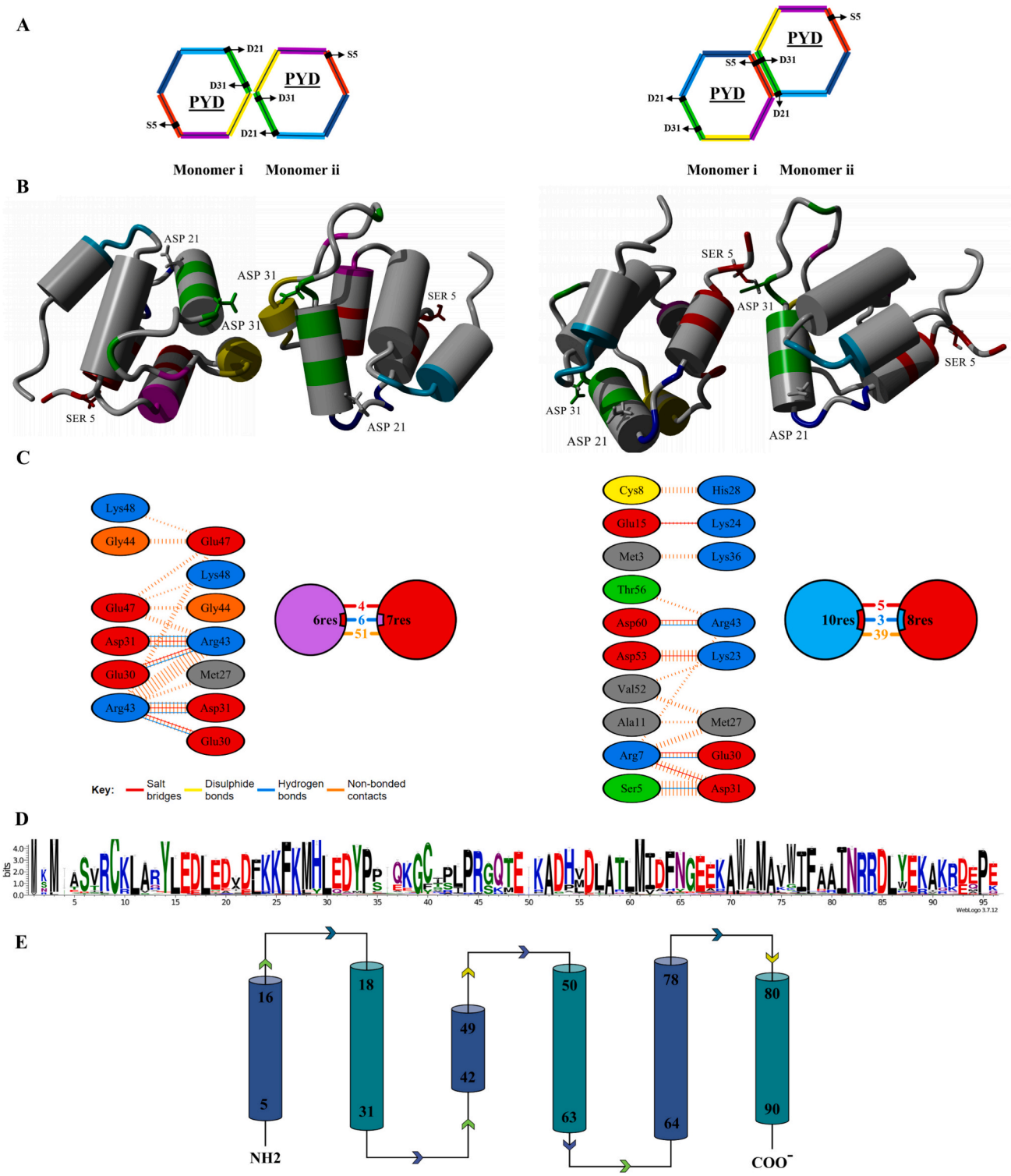

Fig. 1. Overview of representative homotypic interaction geometries of the NLRP3 pyrin domain (PYD). (A) Schematic representation of the PYD contact surfaces involved in the Type A-like model (left; asymmetric IIIa–Ib dimer-like interface) and the representative pairwise Type B-like model selected for downstream comparison (right; Ia–Ib interface organization). Interfaces are colour-coded as follows: Ia (red), Ib (green), IIa (magenta), IIb (cyan), IIIa (yellow), and IIIb (blue). In the Type A-like model, the Ib-containing surface is engaged within a restrained/non-filamentous dimer-like contact, whereas in the representative Type B-like pairwise model, complementary Ia–Ib organization corresponds to the filament-compatible and adaptor-accessible interface observed in published NLRP3 PYD filament and active inflammasome disk structures. This Ia–Ib model was used for direct comparison with the Type A-like dimer and should not be interpreted as the full Type B-like filament or as evidence for a thermodynamically dominant isolated contact. (B) Three-dimensional structural models generated in YASARA illustrating the spatial organization of the two representative geometries. (C) Key interfacial residues identified from PDBsum analysis of representative PYD structures. (D) Sequence conservation of interfacial residues across NLRP3 PYD orthologs visualized using WebLogo. (E) Topological diagram of the PYD highlighting helix organization and residue numbering.

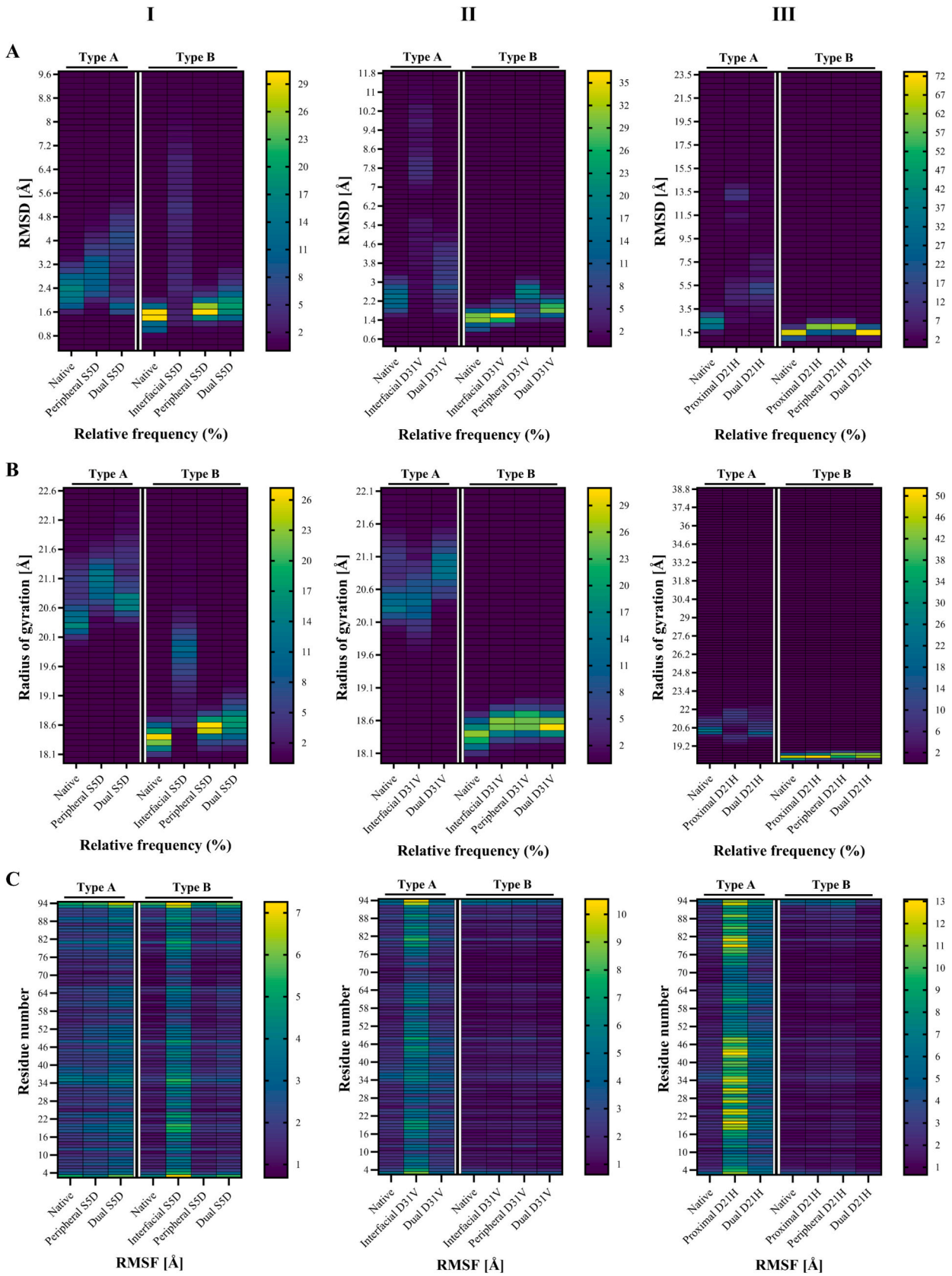

Fig. 2. Dynamic comparison of type A and type B NLRP3 pyrin domain (PYD) interaction modes for S5D (I), D31V (II), and D21H (III) variants. (A) Relative frequency distributions of Cα root-mean-square deviation (RMSD) values, reflecting overall structural stability of the interacting dimers. (B) Distributions of the radius of gyration (Rg), indicating differences in complex compactness between interaction modes. (C) Per-residue root-mean-square fluctuation (RMSF) profiles, illustrating residue-level flexibility across both interacting PYD subunits.

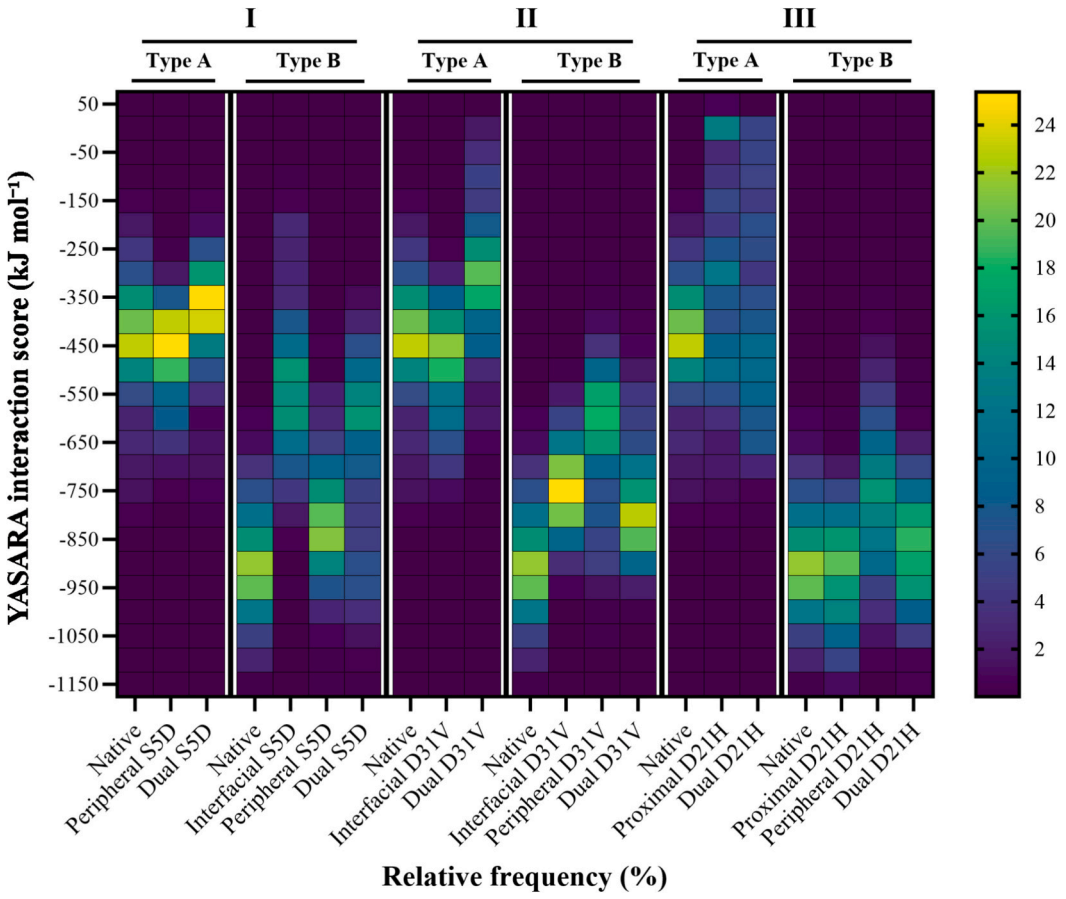

Fig. 3. Comparison of YASARA-derived MM/PBSA-like interaction–solvation scores for native and mutant Type A-like and Type B-like NLRP3 pyrin domain (PYD) interaction models. Panels I, II, and III correspond to S5D, D31V, and D21H variants, respectively. Scores were calculated from molecular dynamics trajectories using the YASARA md_analyzebindenergy macro and are reported in kJ mol^{-1} using the native YASARA sign convention. Within the same analysis framework, shifts toward more negative values were treated only as model-dependent descriptors of greater contact persistence, compactness, and reduced solvent exposure. These scores should not be interpreted as physical binding free energies, absolute thermodynamic affinities, or energetic rankings.

luminescence, consistent with maintained interfacial stabilization (Fig. 4DII; Table 3). (Fig. 4DII; Table 3). Co-expression of NLuc- and CLuc-tagged constructs from a single pETDuet-1 vector reproduced these signal patterns in both lysates and purified samples (Fig. 5III), excluding reassociation artifacts.

ASC recruitment assays further demonstrated that addition of CLuc-ASC to NLuc-PYD S5D reactions failed to enhance luminescence, in contrast to the robust signal increase observed with wild-type PYD (Fig. 6I–II), indicating impaired adaptor engagement.

To independently evaluate soluble low-order association behavior, microscale thermophoresis (MST) was performed on native/native, native/S5D, and S5D/S5D interaction pairs (Fig. 7). Concentration-dependent MST responses were analyzed using the built-in Kd model in MO.Affinity Analysis software, and the resulting values were reported as apparent dissociation constants (Kd,app). The native/S5D heterotypic pair exhibited a lower Kd,app than the native/native interaction (42.6 nM versus 68.1 nM), whereas the S5D/S5D homotypic pair showed a markedly weaker apparent interaction (Kd,app = 514 nM). All measurements were performed under identical experimental conditions, and values are presented as comparative apparent association parameters for soluble low-order PYD interactions rather than absolute thermodynamic binding constants. Furthermore, distinct crossover features were observed in MST response traces for S5D-containing interaction pairs, whereas the wild-type interaction displayed a conventional concentration-dependent response profile.

Mass photometry analysis performed in parallel showed that S5D-containing samples shifted toward smaller low-order soluble species (approximately 52–53 kDa; σ = 12–14 kDa), whereas wild-type CLuc-PYD exhibited a broader and relatively higher-mass distribution of soluble oligomeric states (approximately 76–78 kDa; σ = 25–30 kDa) (Fig. 8).

Collectively, these data revealed distinct effects of S5D substitution across the tested PYD combinations. These observations indicate that the influence of S5D on soluble PYD–PYD association and conformational behavior is dependent on the positional context of the substitution under the examined conditions.

3.2. *D31V uncouples adaptor docking from oligomeric expansion*

NLRP3 PYD polymerization constitutes a key checkpoint during the second stage of inflammasome activation, wherein filament geometry governs ASC recruitment and subsequent elongation. CAPS-associated D31V mutations have produced apparently divergent observations, including reduced homotypic affinity in crystal-like assemblies corresponding to the type A geometry together with enhanced NLRP3–ASC binding [39], as well as impaired self-association in filament-like configurations corresponding to type B [16]. To reconcile these findings, the position-specific effects of D31V were examined across both assembly geometries using all-atom molecular dynamics simulations in conjunction with functional and biophysical assays.

In the type A configuration, where both Asp^{31} residues directly participate in interfacial contacts, single D31V substitution increased conformational dynamics, reflected by elevated Cα-RMSD (6.98 ± 2.54 Å) and RMSF (5.00 ± 1.53 Å) (Fig. 2 AII, CII). Despite increased

Table 3
Percentage of contact types between monomers in native and mutant type A and type B NLRP3^{PYD} assemblies.

Mutation type	Contacts type						
	HB	Hyd	Hyd + HB	Ion	Ion + HB	Ion + Hyd	Ion + Hyd + HB
Type A assembly							
Native	5.96	22.02	1.81	6.09	40.28	4.40	19.43
Peripheral S5D	7.45	12.22	4.32	2.53	57.53	0.30	15.65
Dual S5D	3.69	21.83	2.06	3.10	49.85	2.36	17.11
Interfacial D31V	7.03	25.06	2.34	6.09	41.80	4.33	13.35
Dual D31V	10.46	43.79	4.08	2.94	22.71	1.63	14.38
Proximal D21H	10.61	18.28	3.61	4.51	52.60	0.45	9.93
Dual D21H	9.64	23.22	5.21	3.32	46.92	0.16	11.53
Type B assembly							
Native	38.80	21.63	3.08	1.46	25.17	0.69	9.16
Interfacial S5D	14.77	19.50	1.33	4.87	55.98	0.15	3.40
Peripheral S5D	27.30	25.57	3.93	6.14	27.77	1.10	8.18
Dual S5D	24.78	30.18	4.24	5.11	24.69	1.45	9.55
Interfacial D31V	19.02	28.45	2.69	5.78	33.44	1.11	9.51
Peripheral D31V	31.64	28.36	2.70	2.95	24.67	0.90	8.77
Dual D31V	22.80	25.95	4.27	6.45	31.27	1.05	8.22
Proximal D21H	43.61	19.88	3.25	2.07	21.66	0.30	9.24
Peripheral D21H	32.17	24.79	2.80	2.87	26.03	1.24	10.10
Dual D21H	37.17	21.53	3.42	2.46	24.78	0.87	9.77

flexibility, partial compactness was retained through compensatory interactions and preserved ionic contacts, yielding an interaction score of −493.65 ± 100.21 kJ mol^{-1} (Fig. 3 II; Fig. S7B). Dual D31V substitutions further remodeled the interface, reducing Cα-RMSD to 3.28 ± 0.95 Å while eroding interfacial ionic networks and shifting stabilization toward hydrophobic interactions (interaction score − 303.60 ± 124.85 kJ mol^{-1}; Fig. 3 II; Table 3). Notably, β-sheet formation involving Gln^{35} and Cys^{8} emerged in the dual variant (Fig. S5C), indicating localized secondary structural rearrangement at the interface.

In the type B configuration, where one interfacial Asp^{31} engages Ser^{5} through a stabilizing hydrogen bond, D31V produced geometry-dependent effects. Peripheral substitution resulted in pronounced destabilization, characterized by increased RMSD (2.37 ± 0.48 Å), reduced interaction score (−648.75 ± 125.95 kJ mol^{-1}), and partial unraveling of helix 3 accompanied by loss of interfacial contacts involving residues 15 and 31 (Figs. S8B, S9B; Fig. 3 II). In contrast, interfacial or dual substitutions preserved overall compactness through reinforcement of alternative ionic interactions involving Asp^{50}, Asp^{53}, Asp^{60}, and Glu^{15} (Figs. 2 BII, 9; Table 3). The dual variant exhibited reduced RMSF values (0.63–3.52 Å), driven by hydrophobic packing of Val^{31}, although helix 4 displayed increased lability (Fig. 2CII). These simulations collectively indicate remodeling of electrostatic architecture in a geometry-dependent manner across both assembly states.

Functional consequences of these structural rearrangements were evaluated using split-luciferase complementation assays (Fig. 5 II). All D31V variants exhibited elevated luminescence relative to wild type, with the dual substitution (NLuc-PYD D31V/CLuc-PYD D31V) producing the strongest signal. Co-expression of NLuc-PYD and CLuc-PYD variants from a single pETDuet-1 vector yielded comparable luminescence profiles in lysates and purified samples (Fig. 5 III), confirming that signal enhancement was not attributable to reassociation artifacts. ASC recruitment assays further demonstrated enhanced luminescence upon addition of CLuc-ASC to NLuc-PYD D31V reactions (Fig. 6 II), consistent with increased accessibility of the Ib interface and efficient adaptor docking.

Despite elevated split-luciferase and ASC-recruitment readouts, mass photometry analysis revealed that D31V assemblies remained predominantly confined to smaller soluble low-order species. In contrast to the larger and broader apparent low-order oligomeric distribution observed for wild-type CLuc-PYD (76–78 kDa; σ = 25–30 kDa), D31V variants primarily populated smaller and narrower dimer-like species (52–53 kDa; σ = 12–15 kDa), even after extended incubation (Fig. 8).

Together, these data indicate that D31V increases homotypic and adaptor-associated recruitment readouts while remaining restricted to smaller low-order soluble PYD assemblies relative to the native form.

3.3. *D21H remodels restrained type A-like geometry while preserving ASC-compatible docking*

CAPS-associated D21H mutations are clinically linked to accelerated NLRP3 filamentation and inflammasome hyperactivation [16,40], yet the structural basis of this phenotype remains incompletely defined. Asp^{21} resides at the N-terminus of helix 2, where it participates in intramolecular ionic interactions that contribute to stabilization of the PYD fold. To determine how perturbation at this position influences homotypic assembly, D21H substitutions were evaluated in both Type A-like and Type B-like geometries using molecular dynamics simulations together with complementary functional assays.

In type A dimers, where both Asp^{21} residues are proximal to the interface but engage exclusively in intramolecular interactions (Fig. 1), D21H induced pronounced structural rearrangements. Cα-RMSD increased to 9.70 ± 5.20 Å (Fig. 2 AIII), accompanied by disruption of the Glu^{30}–Asp^{31}–Arg^{43} ionic network (Figs. 3 III, 10A, S7C). Although partial reattachment of this network occurred in alternative conformations, overall interaction score was substantially reduced (Fig. 3 III). Dual D21H substitutions further destabilized the assembly, leading to effective dissociation (Cα-RMSD 6.20 ± 2.71 Å) and dynamic decoupling of helices 2 and 5, as revealed by dynamic cross-correlation analysis (Fig. 10B). Despite these large-scale rearrangements, global secondary structure content remained largely preserved (Fig. S5D). Increased flexibility was observed in helices 2, 3, and 6 (Fig. 2 CIII), consistent with selective destabilization of the type A interfacial organization.

In contrast, type B dimers—where one Asp^{21} residue is proximal to the interface and the other is peripheral (Fig. 1)—remained structurally stable following D21H substitution. All variants exhibited Cα-RMSD values below 2 Å and RMSF values below 2 Å (Fig. 2 AIII, CIII), with near-native binding energies (Fig. 3 III). The dual D21H substitution induced a localized helix-3 coil transition (Fig. S8C), whereas the peripheral variant weakened Asp^{60}-Arg^{43} interactions, resulting in a modest reduction in interaction score (−763 ± 131 kJ mol^{-1}; Fig. S9C). Overall, these simulations indicate selective destabilization of type A assemblies while preserving structural integrity of the type B configuration.

Functional consequences were assessed using split-luciferase complementation assays (Fig. 5 II). Proximal and dual D21H variants produced markedly reduced homotypic NLuc-PYD/CLuc-PYD luminescence relative to wild-type PYD, despite molecular dynamics analyses indicating preservation of Type B-like structural stability. In contrast, peripheral D21H substitution yielded near-native luminescence levels (Fig. 5 II). Co-expression of NLuc-PYD and CLuc-PYD variants from a single pETDuet-1 vector reproduced these signal trends in both lysates and purified samples (Fig. 5 III), excluding reassociation artifacts. ASC-associated recruitment assays demonstrated near-native adaptor engagement for D21H variants (Fig. 6 II), indicating that adaptor-compatible docking competence was retained.

Together, these structural and functional measurements indicate that D21H preferentially perturbs the restrained Type A-like reference model

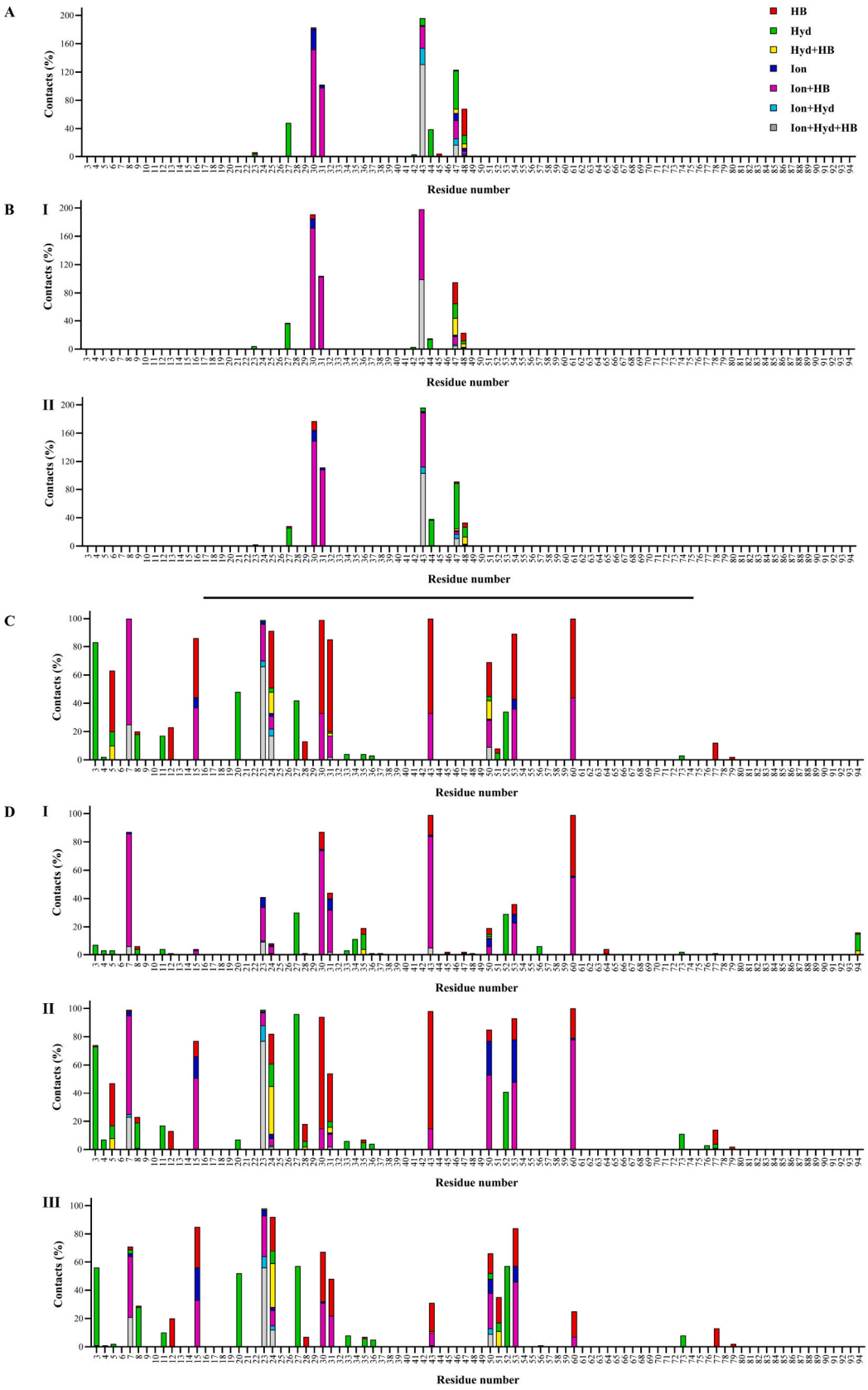

Fig. 4. Interfacial contacts between key residues in native and S5D mutant NLRP3 pyrin domain (PYD) assemblies. (A) Native type A interaction mode. (B) S5D mutant type A assemblies, in which panels I and II represent peripheral and dual substitutions, respectively. (C) Native type B interaction mode. (D) S5D mutant type B assemblies, in which panels I, II, and III correspond to interfacial, peripheral, and dual substitutions, respectively. Inter-residue contacts are classified as hydrogen bonds (red), hydrophobic interactions (green), ionic bonds (blue), and mixed contacts, as indicated in the plot legend.

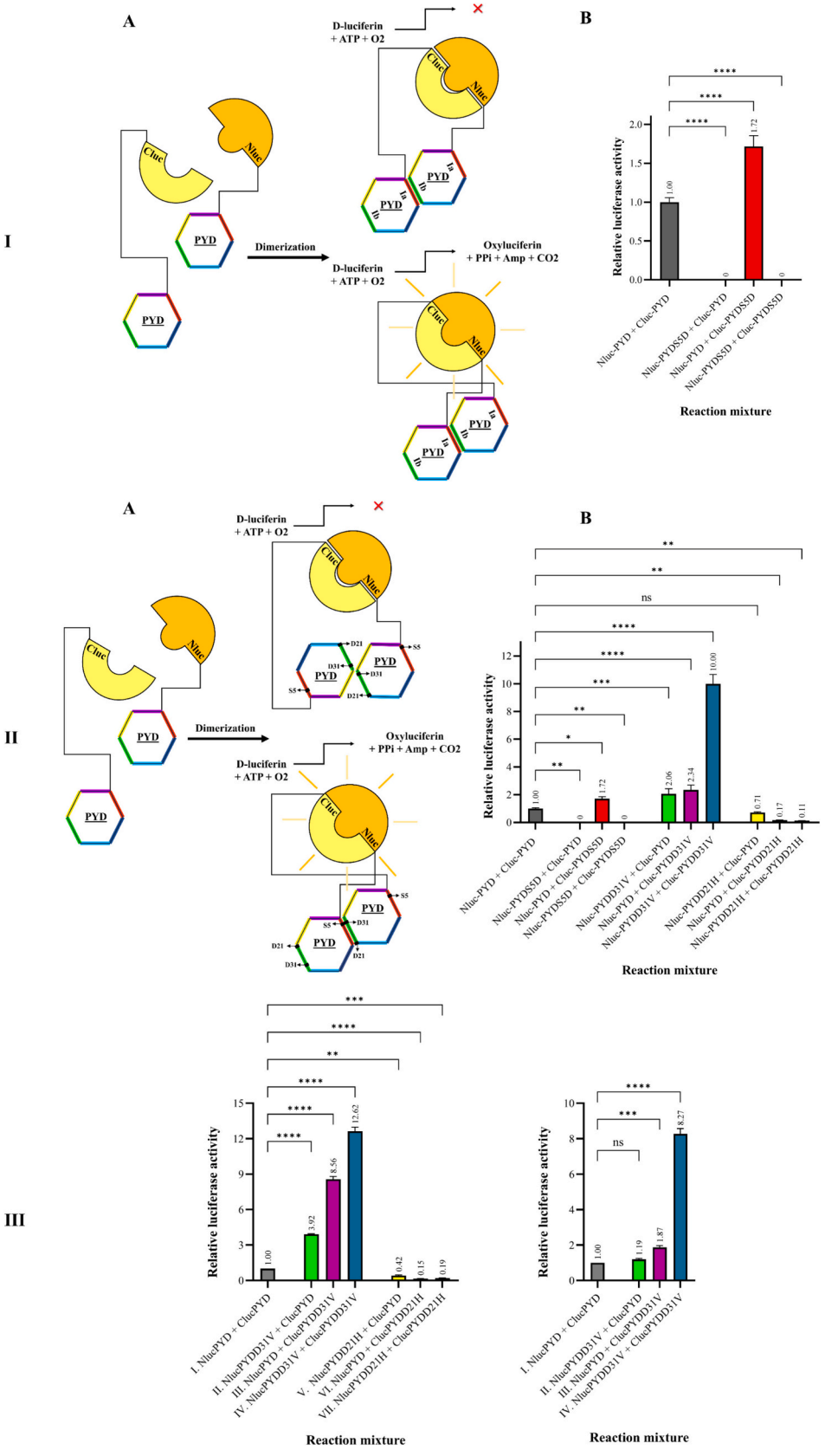

(caption on next page)

Fig. 5. Split-luciferase complementation analysis of reporter-compatible homotypic interactions between native and mutant NLRP3 pyrin domain (PYD) assemblies. (I) Identification of a reporter-compatible Type B-like PYD–PYD register in the split-luciferase system. (A) Schematic representation of two possible type B configurations, in which the Ia interface is positioned on either CLuc-PYD (upper) or NLuc-PYD (lower) at the PYD–PYD contact surface. (B) Luminescence measurements for S5D variants, normalized to the native interaction, demonstrating that only the lower configuration restores reporter activity. (II) Effects of different mutations on PYD assembly. (A) Schematic representation of type A (upper) and type B (lower) interaction modes. (B) Relative luminescence signals for the indicated mutant combinations compared with the native form. (III) Validation of biosensor robustness by co-expression analysis. Luminescence measurements were obtained from cell lysates (left) and from purified proteins (right), yielding results consistent with those from individually expressed constructs and supporting the physiological relevance of the detected interactions. Statistical significance is indicated as follows: * $p < 0.05$, ** $p < 0.01$, *** $p < 0.001$, and **** $p < 0.0001$; ns, not significant.

in simulations, while preserving Type B-like structural stability and ASC-compatible adaptor engagement. The reduced homotypic split-luciferase signal observed for proximal and dual D21H variants should therefore not be interpreted as loss of PYD assembly competence or loss of Type B-like assembly potential. Rather, it indicates that D21H differentially affects homotypic reporter-compatible alignment and ASC-associated adaptor engagement, consistent with the proximity- and orientation-dependent nature of the split-luciferase assay.

4. Discussion

This study supports a geometry-centered framework for NLRP3 PYD self-association, in which the conserved six-helix PYD scaffold can engage alternative homotypic interaction geometries with distinct topological and dynamic consequences. Rather than defining a single obligate PYD–PYD interface, our structural survey, docking analysis, molecular dynamics simulations, and functional readouts indicate that PYD self-association is shaped by interface geometry and local contact chemistry. In this framework, the Type A-like arrangement is best interpreted as a structurally observed, non-filamentous/restrained PYD–PYD reference geometry, represented by the isolated PYD contact [17] and supported by a compatible PYD-dimer arrangement in the inactive CRID3-bound full-length NLRP3 decamer/cage [8]. However, it should not be regarded as an independently proven endogenous regulatory state. By contrast, the Type B-like geometry preserves the complementary Ia–Ib organization observed in NLRP3 PYD filaments [16] and active inflammasome disk structures [38], making it compatible with filament propagation and ASC-accessible assembly. Under identical modeling and analysis conditions, Type B-like dimers displayed greater compactness and more persistent interfacial contacts than Type A-like dimers, while both geometries retained the global PYD fold. Therefore, the functional distinction between these assemblies appears to arise primarily from geometry-dependent interface selection and local electrostatic/hydrogen-bond remodeling, rather than from wholesale destabilization of the PYD domain. This conformational plurality provides a plausible structural basis for how NLRP3 PYD may remain restrained under basal conditions while retaining the capacity to transition toward filament-compatible assembly upon activation.

The S5D phosphomimetic substitution illustrates how a regulatory charge perturbation can modulate NLRP3 PYD self-association in a geometry- and orientation-dependent manner, consistent with previous evidence that Ser5 phosphorylation or phosphomimetic substitution suppresses NLRP3 PYD assembly [15]. In the Type A-like reference geometry, Ser5 is positioned away from the principal IIIa–Ib contact, and molecular dynamics simulations showed that S5D produced only moderate local perturbation: although RMSD increased and localized secondary-structure changes were observed, the core IIIa–Ib contacts remained largely preserved, and the overall radius of gyration was minimally affected. By contrast, in the Type B-like configuration, one Ser5 residue directly contributes to the asymmetric Ia–Ib interface through a Ser5-Asp31 hydrogen bond [16]. Interfacial or dual S5D placement therefore remodeled the local electrostatic and hydrogen-bonding network, reduced intersubunit contact persistence, increased RMSD and RMSF, and expanded the assembly, whereas peripheral S5D placement produced only limited perturbation. This positional asymmetry indicates that the effect of S5D is determined not simply by the presence of a phosphomimetic negative charge, but by whether that charge is introduced into the filament-compatible Ia–Ib contact.

The functional readouts reinforce this interpretation while also defining the interpretive scope of the split-luciferase assay. Because the Type B-like arrangement is asymmetric, alternative NLuc/CLuc reporter orientations can report different PYD registers. S5D placement in NLuc-PYD abolished reporter complementation in both heterotypic and dual-substitution combinations, whereas the reciprocal NLuc-PYD/CLuc-PYD S5D pairing retained, and modestly increased, signal relative to the native interaction. These results support an orientation-dependent model in which a single S5D-containing partner can be accommodated when positioned outside the reporter-sensitive interface, whereas interfacial or dual S5D placement compromises the complementation-compatible register. Importantly, this assay does not directly quantify Type A-like interactions, total Type B-like occupancy, or filament formation; reduced luminescence may reflect either impaired PYD association or altered reporter-fragment spacing within an associated but geometrically remodeled assembly. The inability of CLuc-ASC to enhance luminescence in NLuc-PYD S5D reactions may therefore reflect redistribution away from adaptor-compatible Type B-like organization and toward a more restrained/non-filamentous assembly behavior. However, because Type A-like occupancy is not directly measured in this assay, the more conservative interpretation is that S5D reduces the persistence or accessibility of adaptor-compatible Type B-like surfaces rather than providing direct proof of dominant Type A-like assembly.

The solution-phase measurements further support this position-dependent interpretation. MST showed that the native/S5D heterotypic pair retained strong apparent soluble low-order association, whereas the S5D/S5D homotypic pair displayed substantially weaker apparent association. The crossover behavior observed in S5D-containing MST traces further suggests altered soluble interaction behavior under the assay conditions, rather than a simple uniform weakening of binding. Similarly, mass photometry showed that S5D-containing samples shifted toward smaller soluble low-order species relative to wild type, supporting mutation-dependent redistribution among soluble PYD assemblies without implying direct measurement of extended filament formation. Taken together, the structural, reporter-based, ASC-associated, and solution-phase data indicate that S5D acts as a positional probe of electrostatic sensitivity within the PYD assembly surface. The central mechanistic implication is that Ser5-region negative charge can be tolerated in permissive or peripheral registers but compromises the persistence and accessibility of filament-compatible Ia–Ib organization when placed at the appropriate interfacial position. Thus, S5D does not support a model of wholesale PYD destabilization or directly demonstrate dominant Type A-like occupancy; instead, it reveals how phosphorylation-like charge may bias NLRP3 PYD assembly away from adaptor-accessible, filament-compatible organization through spatially selective remodeling of interfacial contacts.

Whereas Ser5 phosphorylation or phosphomimetic substitution introduces negative charge that can restrict filament-compatible PYD contacts in a position-dependent manner, lysine acetylation may tune the same interfacial landscape through a distinct chemical mechanism. Published studies have shown that NLRP3 acetylation promotes inflammasome assembly and activation, whereas non-acetylatable lysine substitutions within the N-terminal PYD region impair NLRP3 oligomerization- and ASC-associated readouts [11,12]. Although the precise contribution of individual lysines differs among studies, constructs, and activation conditions, the acetylation-sensitive K21/K22/

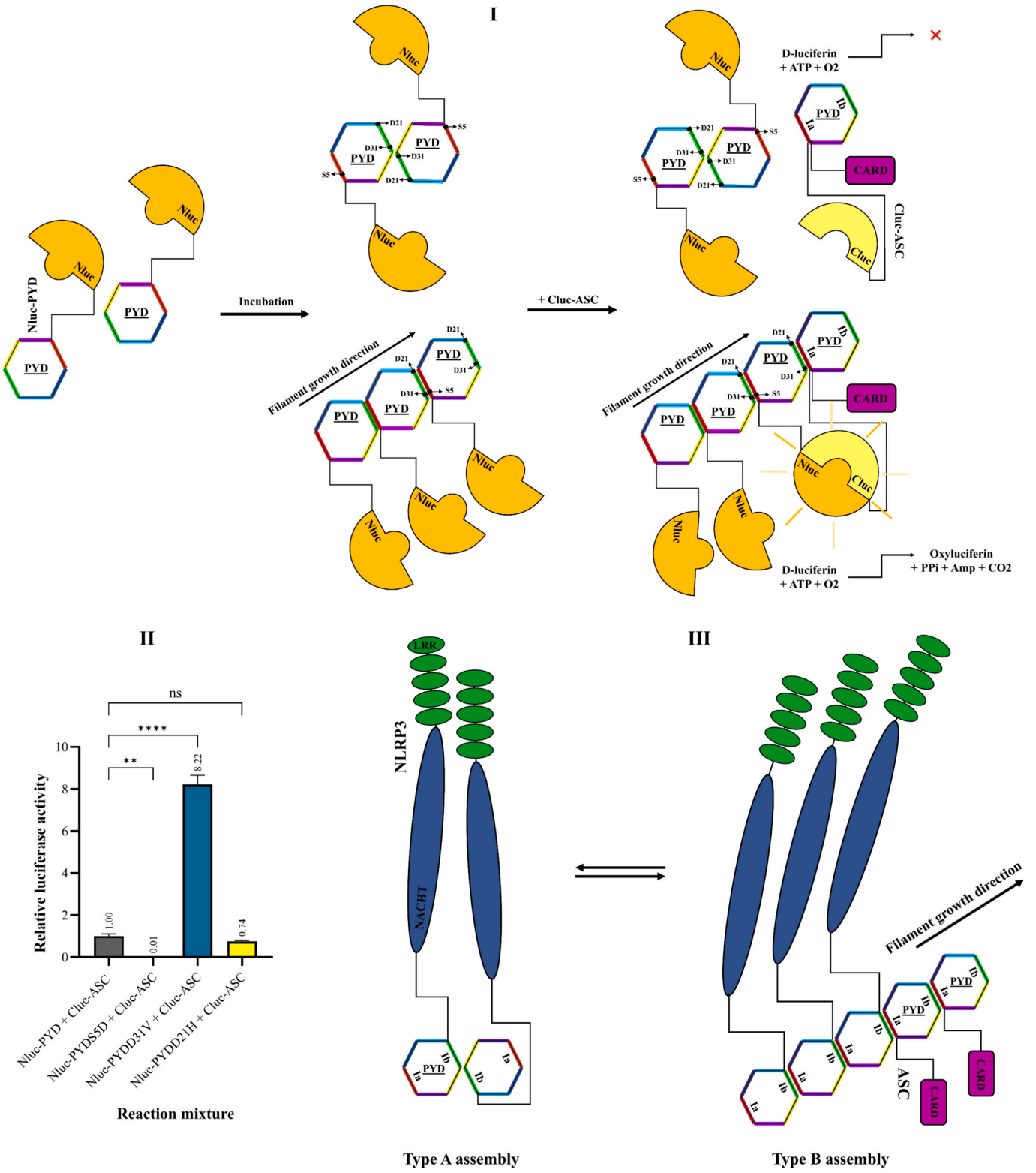

Fig. 6. Functional evaluation of NLRP3 PYD self-association and ASC-compatible adaptor engagement. (I) Schematic representation of the ASC recruitment assay based on the split-luciferase complementation principle. Purified NLuc-PYD variants (native, S5D, D31V, and D21H) were preincubated to allow equilibration of oligomeric states prior to addition of CLuc-ASC. Productive PYD–ASC engagement reconstitutes luciferase activity, enabling quantitative assessment of recruitment efficiency. (II) Quantitative analysis of luminescence measured immediately after mixing with CLuc-ASC and normalized to the native interaction. (III) Proposed model for assembly licensing through conformational switching. The flexible linker connecting the NACHT and pyrin domains facilitates dynamic interconversion between two PYD interaction modes, thereby regulating ASC engagement and supporting downstream inflammasome assembly. Statistical significance is indicated as follows: * $p < 0.05$, ** $p < 0.01$, *** $p < 0.001$, and **** $p < 0.0001$; ns, not significant.

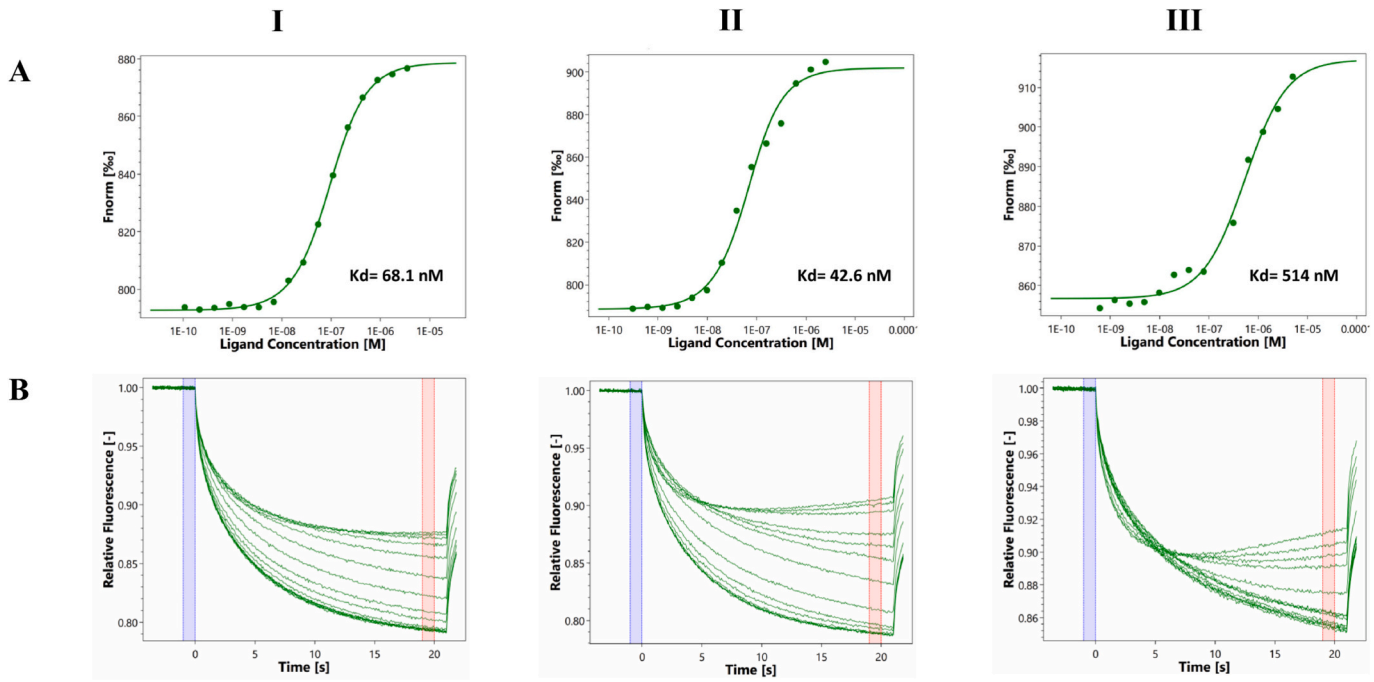

Fig. 7. Microscale thermophoresis (MST) analysis of soluble low-order NLRP3 PYD interaction pairs involving the S5D mutation. Panels I, II, and III correspond to native/native, native/S5D, and S5D/S5D protein mixtures, respectively. (A) Concentration-dependent MST responses showing normalized fluorescence (Fnorm) as a function of unlabeled binding partner concentration. Data points represent measured MST responses, and fitted curves were generated using the built-in Kd model in MO.Affinity Analysis software. Reported values correspond to apparent dissociation constants (Kd,app). (B) Time-resolved MST traces illustrating fluorescence changes during thermophoresis measurements. Blue and red shaded regions indicate initial signal stabilization and thermophoretic response phases, respectively.

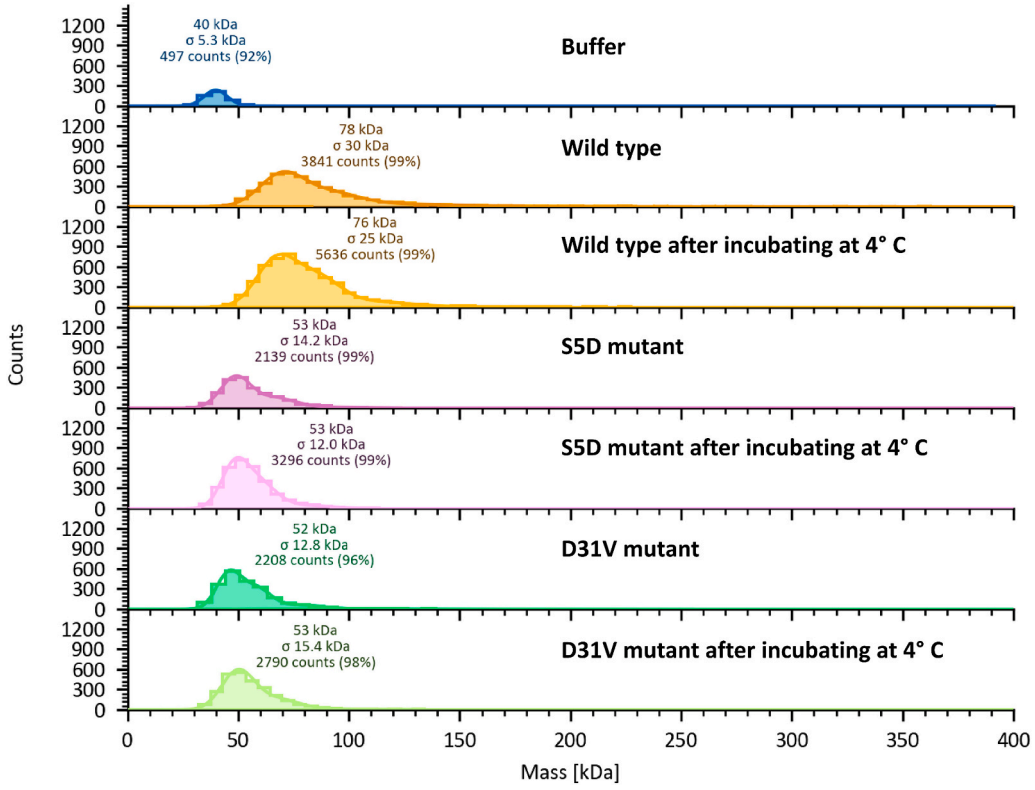

Fig. 8. Mass photometry analysis of low-order soluble NLRP3 PYD assemblies. Wild-type, S5D, and D31V CLuc-PYD variants were analyzed before and after incubation at 4 °C. Mass distribution profiles report the apparent mean molecular mass (kDa), standard deviation (σ), particle count, and relative abundance of detected soluble species for each condition. These data are interpreted as mutation-dependent redistribution among low-order soluble oligomeric states and do not demonstrate extended filament formation.

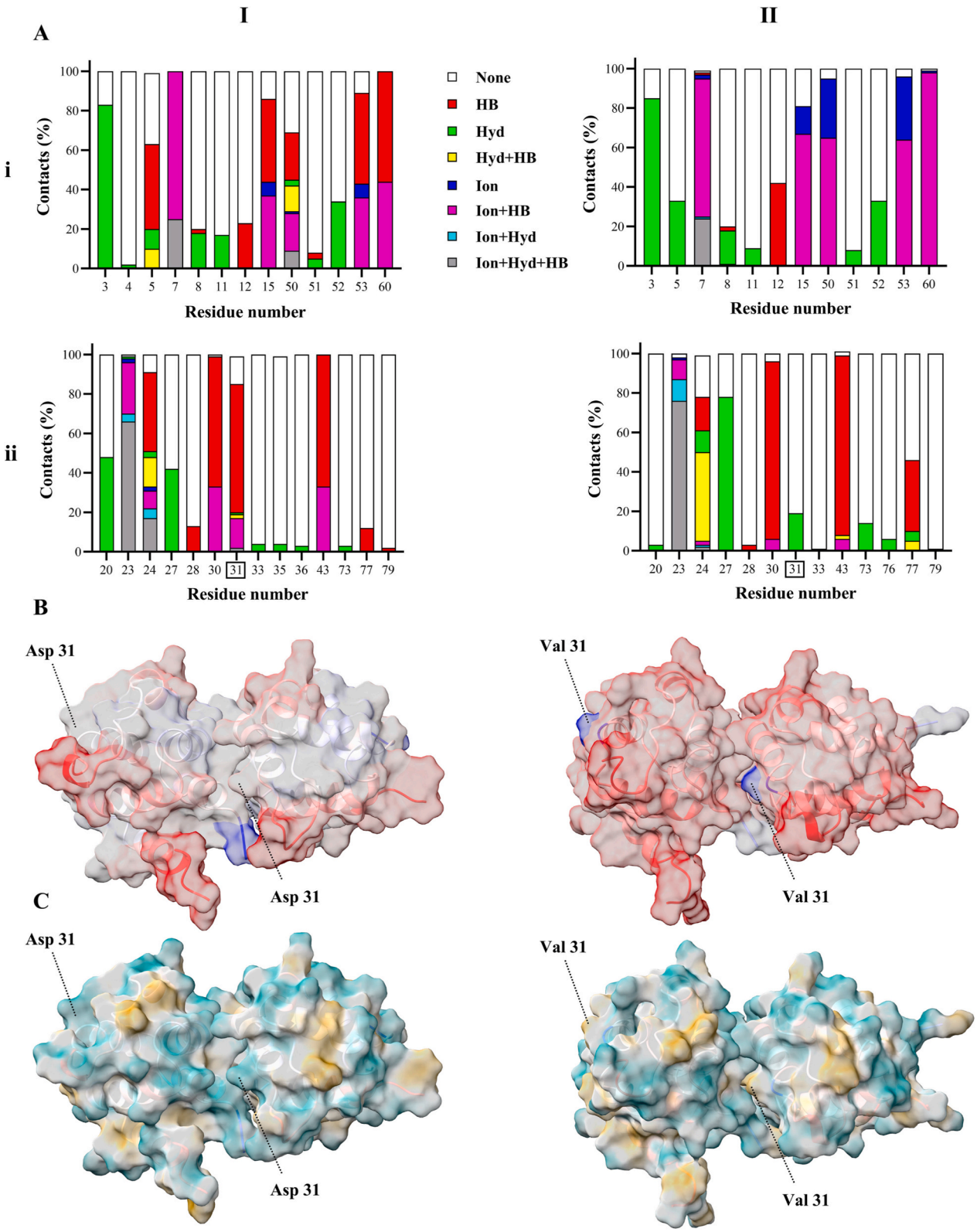

Fig. 9. Structural and interfacial comparison of native (I) and dual D31V mutant (II) type B NLRP3 pyrin domain (PYD) assemblies. Key residues Asp31 and Val31 are highlighted to emphasize mutation-induced alterations at the interface. (A) Intermolecular contact analysis between subunit i and subunit ii during molecular dynamics simulations, illustrating changes in hydrogen bonds, hydrophobic interactions, and ionic contacts. (B) B-factor–based representation of local flexibility mapped onto the assembly surface, where regions of higher flexibility are shown in red and lower flexibility in blue, highlighting dynamic differences between the native and mutant assemblies. (C) Surface hydrophobicity representation, with hydrophobic regions shown in yellow and hydrophilic regions in cyan, illustrating mutation-dependent changes in compactness and interaction potential.

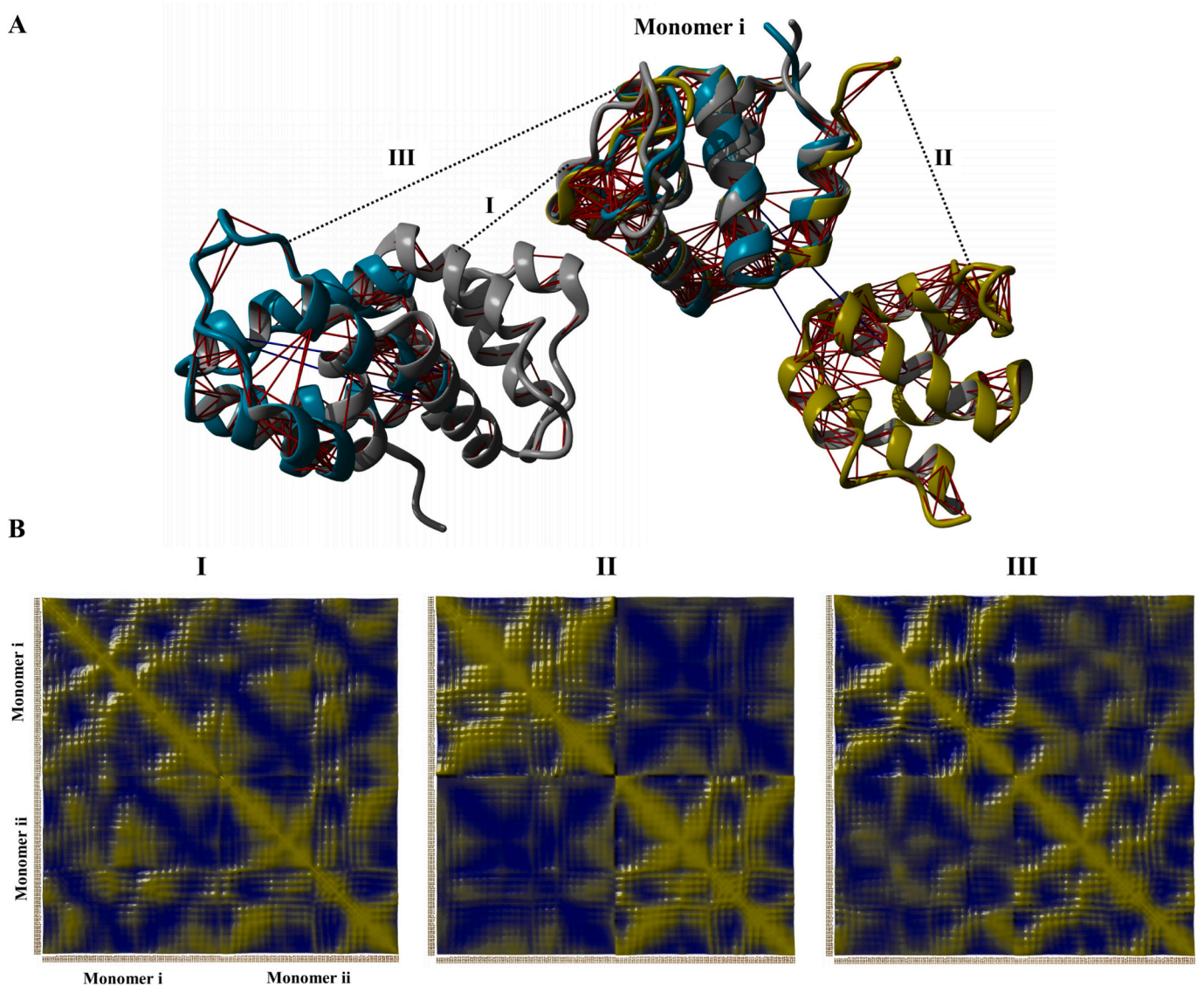

Fig. 10. Residue–residue motion correlations in native (I), proximal (II), and dual (III) D21H mutant type A NLRP3 pyrin domain (PYD) assemblies. (A) Structural representation illustrating inter-residue dynamic correlations, in which blue and red lines denote strongly anticorrelated and correlated residue pairs, respectively. Subunit i from all three assemblies is superposed to facilitate comparison and to highlight mutation-induced changes in the relative motions of subunit ii. (B) Dynamic cross-correlation matrices (DCCMs) derived from molecular dynamics simulations, visualized using a colour scale ranging from blue (−1, fully anti-correlated) to yellow (+1, fully correlated). The matrices illustrate mutation-dependent alterations in correlated motions across the assemblies.

K24 region maps to the N-terminal PYD surface involved in homotypic and adaptor-associated assembly [11,12]. In the present structural framework, the corresponding N-terminal lysine cluster, including Lys23/Lys24 in our model numbering, is positioned within or adjacent to the Ib-containing surface that contributes to filament-associated Ia–Ib organization [16]. Acetylation at this region could therefore alter the local electrostatic, hydrophobic, and steric properties of the interface, thereby influencing the persistence or accessibility of filament-compatible PYD contacts. This possibility appears most directly relevant to Type B-like, filament-compatible organization, whereas effects on Type A-like restrained contacts are expected to be more indirect or context-dependent, because these lysines are not dominant direct contacts in the current Type A-like interaction map. Nevertheless, because Type A-like contacts also involve an Ib-containing surface, acetylation could still modulate restrained geometries by changing local charge distribution or conformational compatibility of the Ib region. Thus, phosphorylation and acetylation may represent chemically distinct PTM inputs that act on neighboring regions of the PYD assembly surface: phosphorylation-like negative charge can constrain filament-compatible contacts, whereas lysine acetylation may promote or permit assembly by remodeling the electrostatic–hydrophobic balance of the N-terminal interface. Future studies using site-specifically acetylated PYD constructs or defined acetylation-mimetic and non-acetylatable variants will be required to determine whether individual acetylation events preferentially increase the persistence or accessibility of filament-compatible Type B-like contacts, indirectly remodel Type A-like restrained contacts, or alter the balance between these interfacial geometries.

In contrast to the phosphomimetic S5D substitution, the CAPS-associated D31V mutation reveals a mechanistic separation between adaptor/proximity-compatible docking and progression into larger soluble PYD assemblies. Asp31 occupies an interfacial electrostatic hotspot within the NLRP3 PYD surface, contributing to the Glu30-Asp31-Arg43-centered contact in the Type A-like geometry and lying within the broader Ia–Ib-associated contact environment of the Type B-like geometry. Replacement of this acidic residue with valine is therefore

expected to remodel local charge distribution, hydrogen-bonding capacity, and hydrophobic surface character without necessarily destabilizing the conserved PYD fold. Consistent with this view, the simulation data indicate geometry-dependent remodeling of Asp31-centered contact networks, including altered ionic interactions in the Type B-like assembly, rather than wholesale structural disruption. These altered ionic and hydrophobic contacts may stabilize a low-order, reporter-compatible PYD register while simultaneously misaligning or restricting the geometry required for cooperative expansion into larger soluble assemblies. Thus, the D31V-induced Type B-like arrangement may remain competent for proximity-based reporter complementation and adaptor-associated docking but less competent for ordered oligomeric progression under the conditions tested.

Functionally, D31V produced a consistent increase in split-luciferase complementation across the tested PYD pairings, with the dual D31V combination yielding the strongest reporter signal. The comparable luminescence profiles observed in co-expression and purified-protein formats further argue against reassociation artifacts and support a genuine increase in reporter-compatible PYD proximity. In parallel, the enhanced CLuc-ASC response in NLuc-PYD D31V reactions is consistent with increased persistence or accessibility of an adaptor-compatible PYD surface. However, these reporter and ASC-associated readouts should not be interpreted as direct measurements of extended filament formation, total Type B-like occupancy, or inflammasome activation. Rather, they indicate that D31V promotes a PYD arrangement that is compatible with reporter complementation and adaptor engagement within the soluble low-order assembly conditions used here.

The mass-photometry data define the key boundary of this interpretation. Despite elevated homotypic reporter and ASC-associated signals, D31V-containing samples remained predominantly confined to smaller soluble low-order species, whereas wild-type CLuc-PYD showed a broader and relatively higher-mass low-order distribution. This behavior is consistent with previous structural and biochemical work showing that the D31V CAPS mutation disrupts ordered NLRP3 PYD polymerization in isolated PYD systems [16]. The present data complement that observation by suggesting that reduced progression into larger soluble PYD assemblies does not necessarily eliminate adaptor-compatible PYD engagement. Instead, D31V appears to uncouple adaptor/proximity-compatible docking from progression into larger soluble PYD assemblies detectable by mass photometry. This distinction provides a plausible mechanistic explanation for the disease relevance of D31V: the mutation may impair coordinated homotypic polymerization while preserving, or even enhancing, local adaptor-compatible interface exposure. Taken together, the structural, reporter-based, ASC-associated, solution-phase, and published polymerization data support a model in which D31V acts not as a simple gain-of-filamentation mutation, but as a CAPS-associated interface-remodeling substitution that biases NLRP3 PYD toward a docking-competent, low-order, geometrically remodeled state. In this model, pathogenic signaling potential may arise from preserved adaptor engagement despite defective ordered PYD polymerization, rather than from unrestricted PYD filament growth.

The CAPS-associated D21H mutation provides a clinically relevant example of how disruption of a restrained PYD contact can be separated from loss of adaptor-compatible assembly potential. Asp21 is located at the N-terminus of helix 2, where it contributes to intramolecular electrostatic stabilization rather than forming a dominant direct intermolecular contact. In the Type A-like reference geometry, however, this region lies close to the restrained dimer-like interface. Molecular dynamics simulations therefore indicate that proximal and dual D21H substitutions selectively remodel this Type A-like geometry: the Glu30-Asp31-Arg43-centered contact network is disrupted or reorganized, intersubunit motions become dynamically decoupled, and the restrained dimer-like arrangement is weakened, while the global six-helix PYD fold remains largely preserved. By contrast, the Type B-like geometry remains structurally stable across D21H placements, with low RMSD/RMSF values and preservation of the overall filament-compatible contact organization under the simulation conditions used. These trajectory-derived observations should not be interpreted as direct measurements of Type A-like or Type B-like occupancy in cells, but they support a topology-based model in which D21H preferentially weakens a restrained/non-filamentous reference geometry while preserving surfaces compatible with adaptor-accessible assembly.

This interpretation is also consistent with published structural and biochemical observations showing that D21H does not behave as a loss-of-function PYD polymerization mutant. Hochheiser et al. reported strong polymerization behavior for D21H NLRP3 PYD, to the extent that gel-filtration/DLS analysis was not feasible, and confirmed this phenotype by negative-stain EM [16]. The same study further showed increased ASC nucleation by D21H in both PYD-only and full-length NLRP3 contexts [16]. Thus, the reduced homotypic NLuc-PYD/CLuc-PYD luminescence observed here for proximal and dual D21H variants should not be taken as evidence that D21H abolishes Type B-like assembly potential. Rather, it highlights the interpretive boundary of the split-luciferase assay. Fragment complementation requires not only PYD–PYD association, but also an appropriate distance, rotational register, and steric arrangement between the NLuc and CLuc fragments. A more extended, reorganized, or filament-compatible PYD assembly can therefore reduce homotypic reporter output if the tagged termini are displaced from the optimal complementation geometry. In this sense, D21H uncouples homotypic reporter-compatible alignment from assembly competence.

The ASC recruitment assay provides the key internal control for this interpretation. In contrast to the reduced homotypic reporter signal, D21H variants retained near-native ASC-associated luminescence after preincubation of NLuc-PYD variants followed by addition of CLuc-ASC. Because ASC engagement depends on the availability of an adaptor-compatible PYD surface, the preserved ASC signal indicates that D21H-containing assemblies retain functionally accessible adaptor-compatible features. This behavior differs from S5D, which perturbs the filament-compatible Ia–Ib interface and strongly reduces ASC-associated signal. Together, the structural, homotypic reporter, ASC-associated, and published polymerization data support a model in which D21H destabilizes or remodels a Type A-like restrained reference geometry while preserving Type B-like adaptor-accessible assembly potential. The apparent decrease in homotypic split-luciferase signal is therefore best explained by altered reporter-fragment alignment within an associated, extended, or reorganized PYD assembly rather than by loss of PYD assembly competence. Importantly, this conclusion remains deliberately bounded: the present assays do not directly quantify Type A-like versus Type B-like occupancy in full-length NLRP3, and direct structural measurement of this redistribution remains an important future goal.

Taken together, the perturbation analyses reveal a coherent but non-binary regulatory logic for NLRP3 PYD assembly. S5D acts as a position-selective phosphomimetic perturbation that preferentially compromises filament-compatible Ia–Ib organization when the introduced negative charge is placed within the appropriate interfacial register. D31V uncouples adaptor/proximity-compatible docking from progression into larger soluble PYD assemblies, producing enhanced reporter and ASC-associated readouts while remaining confined to low-order soluble species under the tested conditions. D21H, in contrast, preferentially remodels the Type A-like restrained reference geometry while preserving Type B-like, adaptor-compatible assembly features, thereby separating homotypic reporter alignment from assembly competence. Across all three cases, the variants do not simply strengthen or weaken PYD self-association as a whole. Instead, they reshape local electrostatic, hydrogen-bonding, and hydrophobic contact networks in a residue-, geometry-, and orientation-dependent manner. This explains why global PYD folding remains largely preserved while reporter complementation, ASC-associated docking, apparent soluble association, and soluble assembly behavior diverge across mutations.

More broadly, these findings support a model in which the NLRP3

PYD functions as a geometry-sensitive interfacial module rather than as a domain controlled by a single obligate self-association surface. Within this framework, Type A-like contacts are best viewed as structurally observed restrained/non-filamentous reference geometries with possible regulatory relevance, not as independently proven endogenous regulatory states. Type B-like organization, by contrast, is grounded in published NLRP3 PYD filament and active inflammasome disk structures and provides the filament-compatible and adaptor-accessible reference geometry. The functional output of PYD perturbations therefore appears to depend on how local chemical changes bias the accessibility, persistence, or register of these alternative interface organizations. This interpretation also accommodates the influence of full-length NLRP3 architecture: flexibility between the NACHT and PYD regions [8] may allow the PYD to sample different restrained and adaptor-compatible arrangements, while upstream licensing events and post-translational modifications tune the likelihood of ASC engagement. Thus, activation competence is better understood as the result of geometry-dependent interface remodeling within a constrained assembly landscape, rather than as a simple binary switch between exposed and hidden PYD surfaces.

This framework identifies several interfacial control points—including Ser^{5}, the N-terminal lysine cluster, Asp^{21}, Glu^{30}, Asp^{31}, Arg^{43}, Asp^{53}, and Asp^{60}—that help coordinate local charge balance, contact persistence, and assembly-register selection within the PYD surface. These residues should not be interpreted as static stabilizers of one universal interface; rather, they function as context-dependent nodes whose effects vary according to geometry, orientation, and assay readout. A key strength of this model is that it assigns each experimental and computational readout to the level of organization it can most directly support: Type A-like and Type B-like arrangements serve as comparative structural reference geometries; trajectory-derived scores describe model-dependent interface behavior; split-luciferase reports complementation-compatible PYD register; ASC-associated luminescence reports adaptor-compatible surface accessibility; MST provides comparative apparent association behavior for soluble low-order PYD interactions; and mass photometry reports soluble low-order oligomeric distributions. By integrating these readouts without treating any single assay as a standalone measure of filament formation or cellular state occupancy, the present study provides a constrained but mechanistically informative map of how regulatory modifications and CAPS-associated mutations reshape NLRP3 PYD assembly. Overall, our findings establish that the conserved six-helix PYD scaffold can preserve its global fold while selectively altering restrained contacts, adaptor-compatible docking, and soluble assembly behavior through residue-level remodeling of interfacial chemistry. This geometry-centered framework offers a structural basis for interpreting NLRP3 PYD regulation and disease-associated perturbations, and provides testable hypotheses for future full-length, post-translationally modified, and time-resolved studies of inflammasome assembly.

5. Conclusion

In conclusion, this study reframes NLRP3 PYD self-association as a geometry-dependent interfacial process rather than a simple on–off transition in homotypic binding. The data support a model in which local electrostatic, hydrogen-bonding, and hydrophobic networks determine whether PYD contacts remain restrained, become adaptor-compatible, or adopt filament-compatible organization, while the conserved six-helix scaffold remains largely preserved. This geometry-centered view provides a mechanistic basis for interpreting how regulatory modifications and CAPS-associated mutations can reshape inflammasome signaling potential through selective remodeling of PYD interfaces. By defining residue-level control points within this assembly landscape, our findings establish a structural rationale for future interface-directed modulation of NLRP3 activity, including strategies aimed at stabilizing restrained PYD contacts or limiting the persistence of adaptor-accessible, filament-compatible interfaces.

CRediT authorship contribution statement

Mehri Javid: Writing – review & editing, Writing – original draft, Visualization, Validation, Software, Project administration, Methodology, Investigation, Formal analysis, Data curation, Conceptualization. **Alexander Dömling:** Writing – review & editing, Validation, Supervision, Resources. **Maryam Nikkhah:** Methodology, Investigation, Data curation. **Grzegorz Popowicz:** Validation, Formal analysis, Data curation. **Mohammad Hashemabadi:** Validation, Methodology, Formal analysis. **Ahmad Reza Shahverdi:** Resources, Project administration. **Zargham Sepehrizadeh:** Resources. **Azadeh Ebrahim-Habibi:** Writing – review & editing, Validation, Supervision, Software, Resources, Project administration, Funding acquisition, Conceptualization. **Saman Hosseinkhani:** Writing – review & editing, Validation, Supervision, Resources, Project administration, Methodology, Funding acquisition, Formal analysis, Conceptualization.

Consent for publication

Not applicable.

Ethics approval and consent to participate

Not applicable.

Funding

This work was supported by the Endocrinology and Metabolism Research Institute, Tehran University of Medical Sciences (Research Code: 67084-221-2-1402), and by the Research Council of Tarbiat Modares University through grant IG/39803 to the Cell Death and Differentiation Research Program. Researcher mobility was supported by the European Commission through the EPIC (Grant No. 690939) and VIDEC (Grant No. 872195) projects. Additional support to A.D. was provided by the ERA Chair grant ACCELERATOR (Grant No. 101087318) and the ERC Advanced Grant AMADEUS (Grant No. 101098001). A.D. also received funding from the National Institute for Cancer Research—Programme EXCELES (Project ID: LX22NPO5102), supported by Cancer Research Czech Republic, and from the Dutch Cancer Society (KWF Kankerbestrijding; Grant No. 14712).

Declaration of competing interest

The authors declare that they have no known competing financial interests or personal relationships that could have appeared to influence the work reported in this paper.

Acknowledgments

During the preparation of this manuscript, the authors used ChatGPT to assist with language editing and improving readability. The authors critically reviewed and edited the content and take full responsibility for the final version of the manuscript.

Appendix A. Supplementary data

The Supporting Information contains supplementary figures and tables providing additional methodological details and extended analyses that support the results presented in the main text. Supplementary data to this article can be found online at https://doi.org/10.1016/j.ijbiomac.2026.153422.

Data availability

No data was used for the research described in the article.

References

[1] K.V. Swanson, M. Deng, J.P.-Y. Ting, The NLRP3 inflammasome: molecular activation and regulation to therapeutics, Nat. Rev. Immunol. 19 (8) (2019) 477–489.
[2] O. Takeuchi, S. Akira, Pattern recognition receptors and inflammation, Cell 140 (6) (2010) 805–820.
[3] M.S. Mangan, et al., Targeting the NLRP3 inflammasome in inflammatory diseases, Nat. Rev. Drug Discov. 17 (8) (2018) 588–606.
[4] C. Ising, et al., NLRP3 inflammasome activation drives tau pathology, Nature 575 (7784) (2019) 669–673.
[5] H.M. Hoffman, et al., Mutation of a new gene encoding a putative pyrin-like protein causes familial cold autoinflammatory syndrome and Muckle–Wells syndrome, Nat. Genet. 29 (3) (2001) 301–305.
[6] Q. Ma, Pharmacological inhibition of the NLRP3 inflammasome: structure, molecular activation, and inhibitor-NLRP3 interaction, Pharmacol. Rev. 75 (3) (2023) 487–520.
[7] J. Fu, H. Wu, Structural mechanisms of NLRP3 inflammasome assembly and activation, Annu. Rev. Immunol. 41 (2023) 301–316.
[8] I.V. Hochheiser, et al., Structure of the NLRP3 decamer bound to the cytokine release inhibitor CRID3, Nature 604 (7904) (2022) 184–189.
[9] K. Schroder, J. Tschopp, The inflammasomes, Cell 140 (6) (2010) 821–832.
[10] A. Gritsenko, et al., Mechanisms of NLRP3 priming in inflammaging and age related diseases, Cytokine Growth Factor Rev. 55 (2020) 15–25.
[11] Y. Zhang, et al., Acetylation is required for full activation of the NLRP3 inflammasome, Nat. Commun. 14 (1) (2023) 8396.
[12] M. He, et al., An acetylation switch of the NLRP3 inflammasome regulates aging-associated chronic inflammation and insulin resistance, Cell Metab. 31 (3) (2020) 580–591.e5.
[13] A. Lu, et al., Unified polymerization mechanism for the assembly of ASC-dependent inflammasomes, Cell 156 (6) (2014) 1193–1206.
[14] M.S. Dick, et al., ASC filament formation serves as a signal amplification mechanism for inflammasomes, Nat. Commun. 7 (1) (2016) 1–13.
[15] A. Stutz, et al., NLRP3 inflammasome assembly is regulated by phosphorylation of the pyrin domain, J. Exp. Med. 214 (6) (2017) 1725–1736.
[16] I.V. Hochheiser, et al., Directionality of PYD filament growth determined by the transition of NLRP3 nucleation seeds to ASC elongation, Sci. Adv. 8 (19) (2022) eabn7583.
[17] J.Y. Bae, H.H. Park, Crystal structure of NALP3 protein pyrin domain (PYD) and its implications in inflammasome assembly, J. Biol. Chem. 286 (45) (2011) 39528–39536.
[18] D.J. Wales, Exploring energy landscapes, Annu. Rev. Phys. Chem. 69 (1) (2018) 401–425.
[19] K. Henzler-Wildman, D. Kern, Dynamic personalities of proteins, Nature 450 (7172) (2007) 964–972.
[20] R. Nussinov, et al., Protein conformational ensembles in function: roles and mechanisms, RSC Chemical Biology 4 (11) (2023) 850–864.
[21] M. Riaz, et al., Predicting multi-interfacial binding mechanisms of NLRP3 and ASC pyrin domains in inflammasome activation, ACS Chem. Neurosci. 12 (4) (2021) 603–612.
[22] A. Hospital, et al., Molecular dynamics simulations: advances and applications, Adv. Appl. Bioinforma. Chem. (2015) 37–47.
[23] S. Hosseinkhani, et al., Harnessing luciferase chemistry in regulated cell death modalities and autophagy: overview and perspectives, Chem. Soc. Rev. (2024) 11557–11589.
[24] T. Azad, A. Tashakor, S. Hosseinkhani, Split-luciferase complementary assay: applications, recent developments, and future perspectives, Anal. Bioanal. Chem. 406 (2014) 5541–5560.
[25] M. Isazadeh, et al., Split-luciferase complementary assay of NLRP3 PYD-PYD interaction indicates inflammasome formation during inflammation, Anal. Biochem. 638 (2022) 114510.
[26] M. Johnson, et al., NCBI BLAST: a better web interface, Nucleic Acids Res. 36 (suppl_2) (2008) W5–W9.
[27] E. Krieger, G. Vriend, YASARA view—molecular graphics for all devices—from smartphones to workstations, Bioinformatics 30 (20) (2014) 2981–2982.
[28] D.T. Jones, Protein secondary structure prediction based on position-specific scoring matrices, J. Mol. Biol. 292 (2) (1999) 195–202.
[29] K. Katoh, J. Rozewicki, K.D. Yamada, MAFFT online service: multiple sequence alignment, interactive sequence choice and visualization, Brief. Bioinform. 20 (4) (2019) 1160–1166.
[30] G.E. Crooks, et al., WebLogo: a sequence logo generator, Genome Res. 14 (6) (2004) 1188–1190.
[31] R.V. Honorato, et al., The HADDOCK2. 4 web server for integrative modeling of biomolecular complexes, Nat. Protoc. (2024) 1–23.
[32] E. Krieger, et al., Improving physical realism, stereochemistry, and side-chain accuracy in homology modeling: four approaches that performed well in CASP8, Proteins Struct. Funct. Bioinform. 77 (S9) (2009) 114–122.
[33] J.A. Maier, et al., ff14SB: improving the accuracy of protein side chain and backbone parameters from ff99SB, J. Chem. Theory Comput. 11 (8) (2015) 3696–3713.
[34] E. Krieger, et al., Assignment of protonation states in proteins and ligands: combining pK a prediction with hydrogen bonding network optimization, Computational Drug Discovery and Design (2012) 405–421.
[35] U. Essmann, et al., A smooth particle mesh Ewald method, J. Chem. Phys. 103 (19) (1995) 8577–8593.
[36] E. Krieger, G. Vriend, New ways to boost molecular dynamics simulations, J. Comput. Chem. 36 (13) (2015) 996–1007.
[37] S. Genheden, U. Ryde, The MM/PBSA and MM/GBSA methods to estimate ligand-binding affinities, Expert Opin. Drug Discov. 10 (5) (2015) 449–461.
[38] L. Xiao, V.G. Magupalli, H. Wu, Cryo-EM structures of the active NLRP3 inflammasome disc, Nature 613 (7944) (2023) 595–600.
[39] J. Hu, et al., A novel mutation in the pyrin domain of the NOD-like receptor family pyrin domain containing protein 3 in Muckle-Wells syndrome, Chin. Med. J. 130 (05) (2017) 586–593.
[40] J.A. Turunen, et al., Keratoendotheliitis fugax hereditaria: a novel cryopyrin-associated periodic syndrome caused by a mutation in the nucleotide-binding domain, leucine-rich repeat family, pyrin domain-containing 3 (NLRP3) gene, Am. J. Ophthalmol. 188 (2018) 41–50.